Microscopic Description of Nuclear Fission at Finite Temperature

A Dissertation

Presented for the

Doctor of Philosophy

Degree

The University of Tennessee, Knoxville

Jordan David McDonnell

August 2012

© by Jordan David McDonnell, 2012
All Rights Reserved.

This dissertation is dedicated to...

Brooke McDonnell, my beloved wife, friend, and sweetest encouragement,

Jeffrey and Kimberly McDonnell,

and Richard and Diane DeBerry

Acknowledgements

I would like to thank Witek Nazarewicz, my adviser who has helped steer me along the way of completing this dissertation. He has been very encouraging throughout the process, identifying aspects of my work that deserved further attention.

I am very grateful to Nicolas Schunck, who tutored me extensively on the theory and programming aspects of the DFT code I used for this dissertation. I have had many conversations with him about career direction, and how to have a successful start in nuclear physics.

I am grateful to Javid Sheikh, Andrzej Staszczak, and Andrzej Baran, who have tutored me in various aspects of finite temperature nuclear theory, fission dynamics, and how to properly conduct a complete study of fission.

I am grateful to Noel Dubray, Daniel Gogny, and Walid Younes. I have had stimulating discussions about nuclear fission with all of them, reminding me about the excitement of pursuing this microscopic theory of fission.

I am very grateful to Carrol Bingham, Robert Grzywacz, Robert Harrison, and Thomas Papenbrock, who served as my doctoral committee. I am thankful for their helpful feedback during my dissertation process.

I am grateful to Jeffrey Way, my physics teacher in high school who helped train me to be attentive to detail and rigorous in math. He taught me a great deal about how to think about science from a Christian view of the world.

I am grateful to Gregory Adkins and Scott Lacey, who invested deeply in me during my undergraduate career. I certainly want to follow in their footsteps and invest in future students just as deeply.

My first year of graduate school was funded in part by the J. Wallace and Katie Dean Fellowship of the University of Tennessee. I am very grateful to the Dean family for their generous gift to the University, and for the study it has allowed me to conduct.

My subsequent work on my dissertation was funded by the Stewardship Science Graduate Fellowship through the Krell Institute and the Department of Energy. I am very grateful to John Ziebarth and Lucille Kilmer for their hard work in administrating this fellowship.

Let the peace of Christ rule in your hearts since as members of one body you were called to peace. And be thankful. Let the Word of Christ dwell in you richly as you teach and admonish one another with all wisdom, and as you sing psalms, hymns, and spiritual songs with gratitude in your hearts to God. And whatever you do, whether in word or deed, do it all in the name of the Lord Jesus, giving thanks to God the Father through Him (Col. 3:15-17).

Abstract

While a predictive, microscopic theory of nuclear fission has been elusive, advances in computational techniques and in our understanding of nuclear structure are allowing us to make significant progress. Through nuclear energy density functional theory, we study the fission of thorium and uranium isotopes in detail. These nuclides have been thought to possess hyperdeformed isomers in the third minima of their potential energy surfaces, but microscopic theories tend to estimate either shallow or non-existent third minima in these nuclei. We seek an explanation in terms of neutron shell effects. We study how the fission pathways, the symmetry, and the third minima of these nuclei evolve with increasing excitation energy. We then study the fission of mercury-180, in which a recent experiment unexpectedly discovered that this nucleus fissions asymmetrically. We find that the fission of mercury-180 and mercury-198 is driven by subtleties in shell effects on the approach to scission. We finally survey fission barrier heights and spontaneous fission half-lives of several actinide nuclei, from radium to californium. For a new energy density functional, we find good agreement between our calculations and available experimental data, lending confidence to the predictions of our theory beyond experimentally measured nuclei.

Contents

List of Tables x

List of Figures xi

1 Introduction 1

1.1 Motivation 1

1.2 Third Minima in Thorium and Uranium Isotopes 4

1.3 Fission of Mercury Isotopes 6

1.4 Survey of Spontaneous Fission in the Actinides 6

1.5 Methodology 7

2 Methods 8

2.1 Self-Consistent Mean Field Theory 8

2.1.1 Nuclear Density Functional Theory 9

2.2 The Finite-Temperature DFT Approach 13

2.3 Constrained Hartree-Fock-Bogoliubov 16

2.4 The DFT Model for Fission 18

2.4.1 Fission Dynamics 19

2.5 Summary 21

3 Third Minima in Thorium and Uranium 23

3.1 Introduction 23

3.2 Potential Energy Surfaces 24

3.3 The Third Minimum through Isotopic Chains 30
3.4 Conclusions 37

4 Study of the Asymmetric Fission of ^{180}Hg **39**
4.1 Introduction 39
4.2 Results 40
4.3 Conclusions 43

5 Survey of Spontaneous Fission in the Actinides **45**
5.1 Introduction 45
5.2 Triaxiality at Second Barrier 46
5.3 Systematic Fission Barrier Heights 49
5.4 Systematics of Spontaneous-Fission Half-lives 54
5.5 Conclusions 56

6 Conclusion **57**
6.1 Third Minima in Thorium and Uranium 57
6.2 Fission in Mercury Isotopes 58
6.3 Survey of Spontaneous Fission in the Actinides 59
6.4 Summary and Prospects 60

7 Specific Contributions **61**

Bibliography **65**

Appendix **72**

A More on ATDHFB **73**

B Tables of Predictions for Spontaneous Fission in the Actinides **78**

Vita **83**

List of Tables

5.1 RMS deviations of theoretical predictions for barrier heights and isomer energies. 54

B.1 First Barrier Heights 79

B.2 Fission Isomer Energies 80

B.3 Second Barrier Heights 81

B.4 Spontaneous Fission Half-lives 82

List of Figures

1.1 Potential energy curves of ^{240}Pu 7

3.1 One-dimensional potential energy curves for ^{232}Th, at several excitation energies 25

3.2 Two-dimensional potential energy surfaces for ^{232}Th, at several excitation energies 26

3.3 Free energy curves and pairing gaps for ^{232}Th at two excitation energies. 27

3.4 Two-dimensional potential energy surfaces for ^{232}U, at several excitation energies 28

3.5 Two-dimensional potential energy surfaces for ^{228}Th, at several excitation energies 29

3.6 Potential energy curves and shell correction energies for $^{226-232}$Th . . 31

3.7 Neutron and proton shell correction energies for $^{226-232}$Th 32

3.8 The potential energy curves and shell correction energies for $^{226-232}$Th, calculated with UNEDF1 33

3.9 Neutron and proton shell correction energies for $^{226-232}$Th, calculated with UNEDF1 34

3.10 The potential energy curves for ^{232}Th, calculated with several functional parametrizations 35

3.11 Potential energy curves and shell correction energies for $^{228-234}$U . . . 36

3.12 Neutron and proton shell correction energies for $^{228-234}$U 37

4.1 The potential energy surfaces for ^{180}Hg at several values ofE^* 40
4.2 The shell correction energies for ^{180}Hg 41
4.3 The potential energy surface for ^{198}Hg at various values of E^* 42
4.4 The shell correction energies for ^{198}Hg. 43

5.1 The potential energy surface of ^{250}Cm, calculated with SkM* 46
5.2 The potential energy surface of ^{250}Cm, calculated with UNEDF1 . . 47
5.3 Shell correction energies for ^{250}Cm, calculated with SkM* 48
5.4 Shell correction energies for ^{250}Cm, calculated with UNEDF1 48
5.5 A comparison between empirical values and predicted values for the inner barrier heights of several actinides 50
5.6 The residuals of the theoretical predictions for the inner barrier heights 51
5.7 A comparison between empirical values and predicted values for the fission isomer energies of several actinides 52
5.8 The residuals for the fission isomer energies 52
5.9 A comparison between empirical values and predicted values for the outer barrier heights of several actinides 53
5.10 The residuals for the outer barrier heights 53
5.11 Predictions for Spontaneous Fission Half-lives in the actinides. 55

Chapter 1

Introduction

Nuclear fission was understood early in terms of the phenomenological liquid drop model (Bohr and Wheeler, 1939), in which the repulsive Coulomb energy of the protons, as atomic number Z increases, overpowers the surface energy that would pull the nucleus towards a spherical shape (Krappe and Pomorski, 2012). Adding single-particle effects dramatically increases the fidelity of the model (see, e.g., (Ring and Schuck, 1980)) – deformed ground states could be described, as well as the possibility of multiple humps in the potential energy on the way to fission (Brack *et al.*, 1972).

We are understanding more about the force that binds the nucleus together from *ab initio* methods (Stoitsov *et al.*, 2010; Bogner *et al.*, 2010), as well as from energy density functionals that attempt to globally capture the qualities of every possible nucleus (Kortelainen *et al.*, 2010). Can we understand fission in terms of these interactions? Can we obtain a microscopic theory of fission that has truly reliable predictive power?

1.1 Motivation

Why do we desire to understand nuclear fission from the standpoint of a purely microscopic theory? The macroscopic-microscopic formalism, in which the nuclear energy is calculated with a liquid drop formula with single-particle effects added

as corrections (Möller *et al.*, 2012a), has certainly been successfully applied to the problem of fission (Möller *et al.*, 2001, 2009; Ćwiok *et al.*, 1994).

On the one hand, the macroscopic-microscopic method has been evolving so that it is very capable of addressing cutting-edge questions in nuclear theory (Möller *et al.* (2012b), for example, presents a case study in the recently discovered asymmetric fission of mercury isotopes). On the other hand, there is uncertainty in the ability of this formalism to extrapolate beyond known regions of the nuclear chart, such as r-process nuclides and the superheavy elements.

In the macroscopic-microscopic method, one calculates the energy levels of protons and neutrons in some mean nuclear potential, which is phenomenologically tuned to obtain realistic results (Cwiok *et al.*, 1987; Möller *et al.*, 2012a). But the nuclear many-body problem is a problem of self-consistency: the nucleons create the potential in which they exist, and the potential influences the motion of the nucleons. The self-consistent mean field theory (Bender *et al.*, 2003) provides the computational techniques necessary to account for this feedback between individual nucleons and the mean field.

The macroscopic-microscopic method, then, serves as an approximation to a completely microscopic theory. The Strutinsky energy theorem (Ring and Schuck, 1980) relates the self-consistent mean field to the components of the macroscopic-microscopic method: the macroscopic component is the smooth, average part of the self-consistent mean field, and the microscopic component arises from the shell correction energies that are very sensitive to nucleon number.

Can a theoretical picture of the nucleus be built "nucleon-by-nucleon?" *Ab initio* methods, such as the no-core shell model, have had recent success for nuclei containing up to about $A = 6$ nucleons (Navrátil and Quaglioni, 2011). Configuration interaction methods and coupled-cluster methods have recently achieved descriptions of nuclei with $A \approx 40$ (Hagen *et al.*, 2010). These techniques become computationally expensive, so that heavier nuclei lie beyond the reach of these techniques at present.

The self-consistent mean field theory allows the nucleus to be studied in a completely microscopic framework, where the mean field is determined by the density-dependent interaction between individual nucleons. This interaction can be obtained with density functional theory (DFT) by optimizing its parameters to global nuclear properties (such as binding energies and radii), nuclear spectroscopy, and properties of the nuclear matter studied in stars (Hebeler *et al.*, 2011; Stone and Reinhard, 2007; Dutra *et al.*, 2012). This opens the door for a theory of fission that is truly predictive – a theory whose input is related only to the force that binds nucleons together, independent of (e.g.) fission barrier data.

Similarly to the way α-decay is understood in terms of the α-particle tunneling through the potential barrier created by the parent nucleus (Viola and Seaborg, 1966), nuclear fission is modeled in terms of the two daughter nuclei tunneling through the potential barrier created by the mutual interaction between the nucleons (Bjørnholm and Lynn, 1980). Experimental quantities, such as the fission cross section and spontaneous fission half-life, can be related to the theoretical probability of tunneling through this potential barrier. But this relationship becomes rather complicated: in order to calculate a cross section, the theory needs to simultaneously provide the potential energy surface, a quantity representing the nucleus' inertia, whether metastable isomeric states might be present (and the competition between γ-decay from these states and fission), and an accounting of single particle excitations.

The potential energy surface is the ingredient most readily yielded by the microscopic, self-consistent approach, so we study potential energy surfaces in detail. Besides comparisons with empirical fission barrier heights and isomer energies, calculating the potential energy surface also reveals the configuration of the nucleus as it fissions, whether it will undergo symmetric or asymmetric fission.

The sequence of shapes a nucleus assumes during the fission process, called the fission pathway, is often determined by an exploration of many degrees of freedom: the length of the nucleus' primary axis (related to the quadrupole moment), the lengths of the minor axes, and the relative sizes of the emerging fragments are among

the primary quantities of interest. It is thought that a self-consistent, variational procedure automatically finds the nuclear shape that minimizes the energy at each point of the fission pathway – but practitioners of the macroscopic-microscopic method contest this assertion (Möller *et al.*, 2009).

The splitting of the potential energy into a series of peaks and valleys, rather than a single hump, comes theoretically as a straightforward consequence of shell corrections (Brack *et al.*, 1972). And rotational bands built on potential minima, associated with superdeformed isomers, have been seen experimentally (see, e.g., Singh *et al.* (2002)). It is typical for the actinides to possess two peaks with one valley in between them. It is also typical for axial symmetry to be broken in the vicinity of the first fission barrier (Pei *et al.*, 2009; Delaroche *et al.*, 2006), and for reflection symmetry to be broken for all points past the first barrier (Möller *et al.*, 2001, 1972).

The details of the potential energy surface are particularly interesting for two subsets of nuclides: thorium and uranium isotopes, in which the question of whether third minima are present has been revisited recently (Kowal and Skalski, 2012); and mercury isotopes, where fission appears to proceed in a manner not expected from extrapolation from the behavior of the actinides (Andreyev *et al.*, 2010).

1.2 Third Minima in Thorium and Uranium Isotopes

The potential energy surfaces for the major actinides, especially Th and U, have an interesting topology. Theorists using various macroscopic-microscopic models (Möller *et al.*, 1972; Ćwiok *et al.*, 1994) predicted a reflection-asymmetric, hyperdeformed isomer in a third potential well, more elongated than known superdeformed isomers. Theoretical calculations performed with microscopic, self-consistent methods typically predict what is topologically a third barrier, but the minimum is very shallow, and

the third barrier often lies well below the second barrier (Bonneau *et al.*, 2004; Berger *et al.*, 1989; McDonnell *et al.*, 2009).

Experimentalists began to see rich resonance structures in fission probabilities for light actinides, particularly isotopes of Th and U, which appeared to be best modeled with moments of inertia corresponding to elongations beyond the superdeformed isomers already understood (Thirolf and Habs, 2002; Krasznahorkay *et al.*, 1999). A cautious discussion of the presence of a hyperdeformed isomer in the third potential minimum began. While band structures were not directly observed in the third potential well, Asghar (1978) observed γ-decay branching ratios that would be fit well by a deep third minimum in the potential. And Blokhin and Soldatov (2009) observed two sets of rotational bands with opposite parity, which would not be possible with only two humps, but would require a third. But the analysis of cross section data is complicated by a large group of closely lying resonances – the analysis of Blokhin and Soldatov (2009), for example, implicitly assumes that vibrations in the second and third potential wells are damped.

Interestingly, the work of Blons *et al.* (1988) comments that their analysis implicitly assumed that the third barrier height is higher than the second – but that fits of like quality can be obtained by assuming the opposite.

There is a conflict between the accepted experimental picture of the third minima and the theoretical picture of most self-consistent studies, as well as the recent macroscopic-microscopic model study of Kowal and Skalski (2012). Is there a physical effect missing from the self-consistent studies? Or is the resolution to be found by examining the optical models employed in the experimental analysis? In Chapter 3, we aim to examine the quality of potential energy surfaces obtained from microscopic, self-consistent calculations for Th and U isotopes. We examine heated nuclei with finite-temperature DFT (FT-DFT), in order to examine the evolution of the balance between shell effects and pairing energy as the pairing energy is reduced with increasing excitation energy.

1.3 Fission of Mercury Isotopes

Since Th and U favor a splitting configuration in which one of the resulting fragments is close to doubly-magic ^{132}Sn, it has generally been understood that the shell structures of the nascent fragments would determine the preferred mass division of a fissioning nucleus. The asymmetric fission of ^{180}Hg, observed by (Andreyev *et al.*, 2010), came as a surprise – the symmetric mass division, corresponding to the semi-magic ^{90}Zr, would seem to be preferred. If the mass division of ^{180}Hg is not determined by the magicity of the nascent fragments, what does drive ^{180}Hg to asymmetric fission?

In Chapter 4, we study the potential energy surfaces of ^{180}Hg and ^{198}Hg, using our study of Th and U as a benchmark. Using FT-DFT, we study of the evolution of the potential energy surfaces as excitation energy increases: do these systems evolve in the same way the actinide nuclei do? Can we learn more about the microscopic forces that surprisingly drive ^{180}Hg to asymmetric fission?

1.4 Survey of Spontaneous Fission in the Actinides

Beyond validating finite-temperature DFT for fission studies, we aim to validate the energy density functional, UNEDF1 (Kortelainen *et al.*, 2012). Since computational technology has improved, this functional was optimized specifically for deformed nuclei, including data for the superdeformed fission isomers of four nuclei. The optimization of this functional to deformed nuclei makes it especially well suited to applications in fission studies.

In Chapter 5, we present fission barrier heights, isomeric energies, and spontaneous fission half-lives for selected even-even major and minor actinides, from Ra to Cf. We compare the results calculated with UNEDF1 to the results of other theoretical predictions, as well as to available empirical data. Our goal is a truly predictive theory of fission – accurate performance of this functional where experimental data

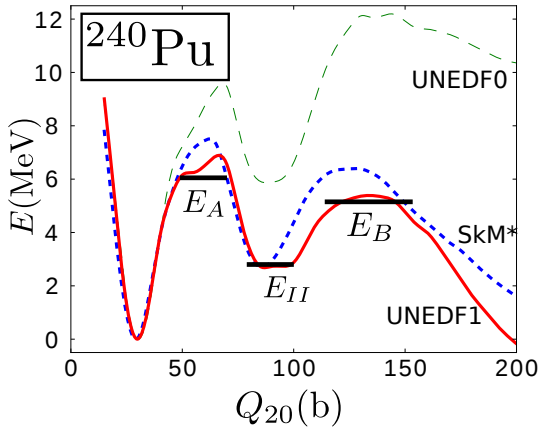


Figure 1.1: The potential energy curves of ^{240}Pu, calculated with several functionals, are shown to highlight the performance of UNEDF1 (figure seen in Kortelainen *et al.* (2012)).

are available is crucial for our confidence in its predictions for hard-to-access nuclei, such as superheavy elements and r-process nuclei.

1.5 Methodology

Before presenting the results of this study, we turn in Chapter 2 to a review of the theoretical and computational techniques employed. We review the density functional theory, briefly describing its foundation in the density-dependent nuclear interaction. We then discuss the finite-temperature Hartree-Fock-Bogoliubov model, which allows fission to be studied as an adiabatic process. We then discuss computational methods, and finally discuss fission dynamics with adiabatic time-dependent HFB.

Chapter 2

Methods

In this chapter, we briefly review the theoretical and computational techniques that are useful for our study of fission.

We review density functional theory and its connection to the microscopic nucleon-nucleon interaction in Section 2.1. In Section 2.2, we then review the generalization of this model to a finite-temperature formalism that can account, for example, for a compound nucleus formed with some excitation energy. We introduce the the mechanisms we use to drive the nucleus to various configurations via constraints in Section 2.3. We then discuss models for the dynamics of fission in Section 2.4, followed by general summarizing remarks in Section 2.5.

2.1 Self-Consistent Mean Field Theory

The goal of this program is a truly predictive theory of fission – that is, a theory that does not fit its parameters to fission-based measurements. The main phenomenological input into our model is the form and parameters of the interaction that binds the nucleons together.

The self-consistent mean field theory, as well as the closely-related density functional theory, has been very successful in calculating the properties of medium-to-heavy mass nuclei (Bender *et al.*, 2003).

The starting point is the Hamiltonian, written in second-quantization notation as

$$H = \sum_{\mu\nu} T_{\mu\nu} C_\mu^\dagger C_\nu + \frac{1}{4} \sum_{\mu\nu\alpha\beta} v_{\mu\nu\alpha\beta} C_\mu^\dagger C_\nu^\dagger C_\beta C_\alpha. \tag{2.1}$$

The $v_{\mu\nu\alpha\beta}$ are the antisymmetrized matrix elements of the two-body, density-dependent potential energy $\mathcal{V}$ derived from the microscopic interaction:

$$v_{\mu\nu\alpha\beta} = \int\int \phi_\mu^*(\vec{r}_1)\phi_\nu^*(\vec{r}_2)\mathcal{V}(\vec{r}_1,\vec{r}_2) \cdot [\phi_\alpha(\vec{r}_1)\phi_\beta(\vec{r}_2) - \phi_\beta(\vec{r}_1)\phi_\alpha(\vec{r}_2)]\, d^3r_1 d^3r_2,$$

where the $\phi_\mu(\vec{r})$ are the single particle wave functions of some basis (the harmonic oscillator basis is often convenient for nuclear physics), expressed as particle creation operators $C_\mu^\dagger$ for the state μ acting on the vacuum state $|0\rangle$

$$\phi_\mu(\vec{r}) = \langle \vec{r} | \, C_\mu^\dagger \, |0\rangle \, .$$

Some form for the two-body interaction $\mathcal{V}$ must then be postulated. Common forms that have proven effective for large nuclei include the zero-range, density-dependent Skyrme interaction (explored by Vautherin and Brink (1972)) or the finite-range Gogny interaction of Dechargé and Gogny (1980).

The Hamiltonian of Eq. 2.1 can be solved only in very special cases. More general cases require the use of the variational principle, arriving at the Hartree-Fock (or Hartree-Fock-Bogoliubov) equations.

Indeed, it is useful to rearrange the expectation value of the Hamiltonian into a form in which the energy of the system is a functional of the local density of the system – the density functional theory.

2.1.1 Nuclear Density Functional Theory

Rather than optimizing the parameters of the two-body potential $\mathcal{V}$ to nuclear data, the philosophy of density functional theory is to adjust the coupling constants of the

nuclear EDF to nuclear data. The universal nuclear EDF (UNEDF) has been put forward in an attempt to describe the properties and reactions of nuclei across the nuclear chart Kortelainen *et al.* (2010).

The energy functional E is written as a functional of the density $\rho(r)$ and pairing density $\tilde{\rho}(r)$, decomposed into kinetic energy density $\mathcal{E}_{\text{kin.}}$, nuclear particle-hole interaction energy density $\mathcal{E}_{\text{int.}}$, pairing energy density $\mathcal{E}_{\text{pair}}$, and Coulomb energy density $\mathcal{E}_{\text{Coul.}}$:

$$E[\rho,\tilde{\rho}] = \int d^3r \left\{\mathcal{E}_{\text{kin.}}(r) + \mathcal{E}_{\text{int.}}(r) + \mathcal{E}_{\text{pair}}(r) + \mathcal{E}_{\text{Coul.}}(r)\right\} \tag{2.2}$$

(see, for example, Kortelainen *et al.* (2012), Stone and Reinhard (2007), and Bender *et al.* (2003)). The optimization of the theory to experimental data occurs in the $\mathcal{E}_{\text{int.}}$ and $\mathcal{E}_{\text{pair}}$ terms. For the interaction energy density $\mathcal{E}_{\text{int.}}$,

$$\begin{aligned}\mathcal{E}_{\text{int.}}(r) = \sum_{t=0,1} \quad & \Big\{C_t^{\rho\rho}\rho_t^2 + C_t^{\rho\tau}\rho_t\tau_t + C_t^{J^2}\mathbf{J}_t^2 \\ + \quad & C_t^{\rho\Delta\rho}\rho_t\Delta\rho_t + C_t^{\rho\nabla J}\rho_t\nabla\cdot\mathbf{J}_t\Big\},\end{aligned} \tag{2.3}$$

where ρ_t, $\mathbf{J}_t$, and τ_t are respectively the particle density, spin-orbit density, and kinetic-energy density corresponding to isospin t. The low-energy coupling constants, C, multiplying each term are adjusted to fit experimental data, such as binding energies and radii. The $t = 0$ terms correspond to isoscalar ($\rho_0 = \rho_n + \rho_p$) contributions, and the $t = 1$ terms correspond to isovector ($\rho_1 = \rho_n - \rho_p$) contributions.

For the pairing energy density $\mathcal{E}_{\text{pair}}$, one often applies the density-dependent ansatz

$$\mathcal{E}_{\text{pair}}(r) = \sum_{q=n,p} \frac{V_0^q}{2}\left\{1 - \frac{\rho_0(r)}{2\rho_c}\right\}\tilde{\rho}^2(r), \tag{2.4}$$

where the V_0^q are the pairing interactions strengths that are chosen to reproduce the pairing gaps that can be extracted from odd-even mass differences. Because pairing can change dramatically across the nuclear chart, most functionals do not explicitly prescribe the V_0^q parameters – for example, our calculations with SkM* are performed with V_0^q adjusted for the pairing gaps taken from ^{232}Th (for the thorium/uranium study, as well as for the actinide survey) or from ^{180}Hg (for the study of the fission of mercury isotopes). More recent functionals, including UNEDF1, do prescribe the V_0^q parameters.

One goal of the UNEDF program is to provide a framework for a predictive theory of fission. When the first pass of the UNEDF fit was found to have incorrect behavior for highly deformed nuclei, a second fit by Kortelainen *et al.* (2012) produced a functional that seems to be very viable for fission applications. Chapter 5 of this thesis is devoted to evaluating the performance of this functional in calculating fission barriers and spontaneous fission half-lives in the actinide region.

To determine the nuclear configuration and energies for a given nucleus and functional (corresponding to the eigenvalues and eigenfunctions of the Hamiltonian Eq. 2.1), the energy density Eq. 2.2 is varied with respect to the densities. The result of this variation (when pairing is fully included) is the Hartree-Fock-Bogoliubov equation (Ring and Schuck, 1980):

$$\sum_k \begin{bmatrix} h_{ik} & \Delta_{ik} \\ -\Delta_{ik}^* & -h_{ik}^* \end{bmatrix} \begin{bmatrix} U_{kj} \\ V_{kj} \end{bmatrix} = E_j \begin{bmatrix} U_{ij} \\ V_{ij} \end{bmatrix}. \tag{2.5}$$

The U and V matrices are the coefficients of the Bogoliubov transformation that relates the particle creation operators $C_\mu^\dagger$ to *quasi-particle* creation operators $a_i^\dagger$:

$$\begin{bmatrix} a_i \\ a_i^\dagger \end{bmatrix} = \sum_\mu \begin{bmatrix} U_{i\mu}^\dagger & V_{i\mu}^\dagger \\ V_{i\mu}^T & U_{i\mu}^T \end{bmatrix} \begin{bmatrix} C_\mu \\ C_\mu^\dagger \end{bmatrix}, \tag{2.6}$$

The ground state eigenfunction $|\Phi_{\mathrm{HFB}}\rangle$ is a quasi-particle vacuum, so that

$$a_i \, |\Phi_{\mathrm{HFB}}\rangle = 0$$

for all i.

The h is the mean-field (particle-hole) part of the Hamiltonian. It takes the form

$$h_{ij} = (\epsilon_i - \lambda_i)\delta_{ij} + \Gamma_{ij},$$

where

$$\Gamma_{ij} = \sum_{k\ell} v_{ikj\ell}\rho_{\ell k},$$

ϵ_i are the single-particle internal energies, and λ_i are the chemical potentials. The Δ is the pairing (particle-particle) part of the Hamiltonian, taking the form

$$\Delta_{ij} = \frac{1}{2}\sum_{k\ell} v_{ijk\ell}\kappa_{k\ell}.$$

The ρ and κ occurring in the definitions of Γ and Δ are respectively the density matrix and pairing tensor:

$$\rho_{ij} = \left\langle C_j^\dagger C_i \right\rangle = \sum_k \left(V_{ik}^* V_{kj}^T\right), \tag{2.7}$$

$$\kappa_{ij} = \langle C_j C_i \rangle = \sum_k \left(V_{ik}^* U_{kj}^T\right). \tag{2.8}$$

They are connected with the densities ρ and $\tilde{\rho}$ occurring in the definition of the energy density functional Eq. 2.2 (Dobaczewski *et al.*, 1984).

The average pairing gap, related to experimental odd-even mass differences, is connected to Δ defined above (Dobaczewski *et al.*, 2009):

$$\overline{\Delta} = \frac{\sum_{ij} \Delta_{ij}\rho_{j\bar{i}}}{\sum_i \rho_{ii}},$$

where $\bar{i}$ denotes the time-reversal of the state i.

The energy density functional can be related to the components of the macroscopic-microscopic energy through the Strutinski energy theorem (Ring and Schuck, 1980; Nikolov *et al.*, 2011; Vertse *et al.*, 2000),

$$E = E_{\text{smooth}} + \delta E^{\text{sh.}},$$

where E_{smooth} is a liquid-drop-like contribution to the energy that varies smoothly with nucleon number, and $\delta E^{\text{sh.}}$ is a shell correction energy that varies rapidly with nucleon number. Two methods are available for the calculation of $\delta E^{\text{sh.}}$ (Schunck *et al.*, 2012): the first method averages individual Hartree-Fock energies of the occupied single particle states, while the second method also subtracts spurious contributions from positive-energy states (which is particularly significant near driplines). Both methods are parametrized by smoothing widths $\gamma_{n,p}$ for neutrons and protons, respectively, and by a curvature correction p. For the actinides (where nuclei were not near driplines), we used the first method, with $\gamma_p = \gamma_n = 1.20$ and $p = 6$. For mercury, we used the second method with $\gamma_n = 1.66$, $\gamma_p = 1.20$, and $p = 10$.

The density matrix ρ and pairing tensor κ can be conveniently packaged into a generalized density matrix

$$\mathcal{R} = \begin{bmatrix} \rho & -\kappa \\ \kappa^* & 1-\rho^* \end{bmatrix}. \tag{2.9}$$

This matrix commutes with the HFB matrix, so that both matrices are diagonalized by the same representation.

Eq. 2.5 is solved through iterative diagonalization until self-consistency is achieved.

2.2 The Finite-Temperature DFT Approach

The self-consistent mean-field formalism is sufficient to study spontaneous fission from a nucleus' ground state. Of course, a nucleus in a realistic environment is not always

in its ground state. A compound nucleus, formed perhaps by neutron capture or by the fusion of two smaller nuclei, most frequently exists in an excited state. As such, it is useful to consider a microscopic model that can account for this excitation energy.

The finite-temperature Hartree-Fock-Bogoliubov (FT-HFB) theory is a straightforward generalization of the normal HFB theory that readily incorporates a statistical ensemble of excited states. The theory can be derived by minimizing a grand canonical potential (Goodman, 1981), after which one arrives at equations that are formally identical to the ordinary HFB equations (Egido *et al.*, 1986).

Rather than a single reference wave function $|\Phi_{\mathrm{HFB}}\rangle$, the FT-DFT approach obtains expectation values of operators through the statistical density operator D:

$$\left\langle \hat{A} \right\rangle = \mathrm{Tr}\left(D\hat{A} \right),$$

where the trace is taken over all possible configurations and $\hat{A}$ is some operator. The energy density functional Eq. 2.2 then enters the grand canonical potential,

$$\Omega = E - TS - \lambda N,$$

which also involves temperature T, entropy S, chemical potential λ, and particle number N.

The entropy S is defined as

$$S = -kD \ln D.$$

The minimization of Ω leads to the finite temperature HFB equations, which have a form identical to Eq. 2.5. The difference in the FT-HFB theory for $kT > 0$MeV occurs in the definition of the density and pairing tensors:

$$\rho_{ij} = \left\langle C_j^\dagger C_i \right\rangle = \sum_k \left(U_{ik} f_k U_{kj}^\dagger + V_{ik}^* (1-f)_k V_{kj}^T \right), \tag{2.10}$$

$$\kappa_{ij} = \langle C_j C_i \rangle = \sum_k \left(U_{ik} f_k V_{kj}^\dagger + V_{ik}^* (1-f)_k U_{kj}^T \right), \tag{2.11}$$

with the Fermi distribution function defined in terms of the inverse temperature $\beta = \frac{1}{kT}$,

$$f_i = \frac{1}{1 + e^{\beta E_i}}.$$

In terms of the Fermi distribution function, the entropy S can be calculated more straightforwardly:

$$S = -k \sum_i \left[f_i \ln f_i + (1 - f_i) \ln(1 - f_i) \right].$$

Because these equations and the corresponding FT-HFB equations were derived from a grand canonical ensemble, the energies obtained from solving the eigenvalue problem Eq. 2.5 are calculated at a fixed temperature. Fission is not isothermal, since there is no heat bath; but since the large-amplitude collective motion is much slower than the single-particle motion, it is reasonable to treat fission as an adiabatic process (Nazarewicz, 1993). But there is a correspondence between surfaces of free energy ($F = E - TS$) at constant temperature to surfaces of internal energy at constant entropy (Pei *et al.*, 2009). We therefore calculate the free energy for a fixed temperature as a function of the collective coordinates, understanding that relative quantities such as barrier heights will identically match those obtained from a calculation of internal energy at fixed entropy.

Furthermore, we map the excitation energy of the nucleus E^* to the fixed temperature T via

$$E^*(T) = E_{\text{g.s.}}(T) - E_{\text{g.s.}}(T = 0),$$

where $E_{\text{g.s.}}(T)$ is the minimum energy of the nucleus at temperature T. This corresponds well to the excitation energy of a compound nucleus formed through such processes as heavy-ion fusion, induced fission, and electron capture (Pei *et al.*, 2009; Sheikh *et al.*, 2009).

2.3 Constrained Hartree-Fock-Bogoliubov

Because the HFB equations arise from a variational principle, the solution will locate the ground state of the system. In order to drive the system from its ground state to a fission configuration, we use the technique of Lagrange multipliers to constrain the system's configuration, so that different nuclear shapes can be explored.

Historically, coupling the microscopic single-particle motion to collective degrees of freedom was engineered through physical intuition gained from the variants of the macroscopic-microscopic model. Following this cue, we choose to constrain the expectation values of multipole moment operators - namely, Q_{20} (elongation), Q_{22} (triaxiality), and Q_{30} (reflection asymmetry). The multipole moments $Q_{\lambda\mu}$ are defined as

$$Q_{\lambda\mu} = a_{\lambda\mu} \int \rho(\vec{r}) r^{\lambda} Y^{*}(\theta, \phi) d^{3}r,$$

where the $a_{\lambda\mu}$ are normalization constants defined by Dobaczewski and Olbratowski (2004).

If a given constrained quantity (represented by the operator $\hat{Q}_i$) has the expectation value $q_i^{(n)} = \left\langle \hat{Q}_i \right\rangle$ at iteration n, and a desired value of q_i, we constrain our HFB solutions by adding a quadratic penalty function to the h functions above,

$$h' = h + \sum_i C_i \left(q_i^{(n)} - q_i \right)^2,$$

with a stiffness constant C_i. The quadratic penalty function, however, does not guarantee that the calculation will converge in every region of the configuration space to be explored. For example, the region near the saddle points requires a high value of the stiffness constant, which can destabilize the self-consistent iteration.

We have explored alternative algorithms to overcome this difficulty. One method is the augmented Lagrangian method (Staszczak *et al.*, 2010), in which the h function adopts the form

$$h'_{A.L.} = h' + a_i^{(n)} \left(q_i^{(n)} - q_i \right),$$

and the $a_i^{(n)}$ are updated with each iteration of the calculation according to

$$a_i^{(n+1)} = a_i^{(n)} + 2C_i \left(q_i^{(n)} - q_i \right).$$

Our studies indicate that, while this method affords extremely precise control over the constrained coordinate (the expectation value matches the requested value with a precision on the order of 1×10^{-4}), this precision comes at the price of extended computational time.

Another algorithm comes from the theory group at Lawrence Livermore National Laboratory (Younes and Gogny, 2009). It is an approach that uses only linear constraints (so the $C_i = 0$ above), where the Lagrange multipliers are adjusted through an RPA calculation at each iteration. The Lagrange multipliers are updated from iteration $n-1$ to iteration n according to

$$\lambda_i^{(n)} = \lambda_i^{(n-1)} + \sum_j (T^{-1})_{ij} (q_j - q_j^{(n)}).$$

The matrix T_{ij} is defined as

$$T_{ij} = \frac{1}{2} \vec{Q}_i (M^{-1} \vec{Q}_j),$$

where the vector bars denote that the $\hat{Q}_i$ is decomposed into a two-block representation (wherein the density operator is diagonalized) and M is a matrix related to the linear response of the density matrix according to QRPA:

$$M^{-1} = \begin{bmatrix} [(\epsilon_\mu + \epsilon_\nu)^{-1} \delta_{\mu\sigma} \delta_{\nu\tau}] & [0] \\ [0] & [(\epsilon_\mu + \epsilon_\nu)^{-1} \delta_{\mu\sigma} \delta_{\nu\tau}] \end{bmatrix}.$$

(These equations are quoted from Younes and Gogny (2009), presented here for the completeness of the review.) In practice, we found that the RPA constraint algorithm led to accurate solutions more quickly than the augmented Lagrangian

method. But since the RPA constraint algorithm has not yet been implemented for finite temperature calculations, we found the augmented Lagrangian method helpful for finite temperature calculations.

The code HFODD (Dobaczewski and Olbratowski, 2004; Schunck *et al.*, 2012) solves the HFB equations by expressing the trial wave functions through their expansion in a harmonic oscillator basis, and the basis functions are expressed in Cartesian coordinate space. The iterative solution is begun by postulating a form for the mean field (often of a Nilsson form), then solving the HFB equations to obtain the densities. These densities are then used to compute the mean field for the next round of the iteration procedure. The iterations continue until the input and output mean fields and densities are equivalent (to within a specified numerical precision).

Our calculations are performed with the program HFODD v2.49t, which implements finite-temperature HFB, as well as the augmented Lagrangian method and the RPA constraint methods. Our calculations use the RPA constraint method for zero-temperature calculations, and we use the augmented Lagrangian method for finite-temperature calculations.

2.4 The DFT Model for Fission

With the constrained HFB calculations, the potential energy is mapped as a function of the constraining coordinates to obtain a potential energy surface. The potential energy surface is a major ingredient for the estimation of fission observables. It is common practice to approximate fission as a one-dimensional barrier penetration problem (Bjørnholm and Lynn, 1980). Variations of the WKB approximation can be used to calculate the probability of tunneling through the barrier. The tunneling probability determines the half-life for spontaneous fission, and the cross section for induced fission.

This approach is semi-classical: the potential energy barrier through which the system tunnels is calculated with the full self-consistent mean field theory, while the

system is often assumed to traverse along the path of least action. This semi-classical approximation is appropriate because the collective motion of the nucleus towards fission is slow compared to the motion of single particles.

The action along that trajectory (Baran *et al.*, 2007),

$$S = \int_{(s)} \left\{ 2[V(q) - E] \sum_{ij} \mathcal{M}_{ij}(q) \frac{dq_i}{ds} \frac{dq_j}{ds} \right\}^{1/2} ds, \tag{2.12}$$

where s is the coordinate along the trajectory, q_i are the collective coordinates describing the nuclear configuration, $V(q)$ the potential energy (corrected by a zero-point energy), E the ground state energy, and $\mathcal{M}_{ij}$ the collective inertia.

A fully quantum mechanical treatment could be achieved via a path integral for each possible path from ground state to scission (Negele, 1989; Skalski, 2008), but this is beyond the reach of current computational technology.

Experimentalists can measure cross sections of induced fission reactions. They can estimate fission barriers by assuming a one-dimensional potential energy curve in the form of stitched-together parabolic curves. The fission barrier heights are estimated by adjusting the parameters of the parabolic curves to reproduce the cross section data.

Several assumptions enter such a procedure. The calculations are done with an optical model that requires assumptions about the effects of isomeric minima in the potential energy surface, such as absorption. But the parameters of this optical model are phenomenological, and there is plenty of room for adjustment – for example, some analyses infer a third minimum in the potential energy surface of ^{232}Th, while others suggest instead that the resonances are caused by single-particle level crossings (Mirea *et al.*, 2007).

2.4.1 Fission Dynamics

One useful approach to fission dynamics is the adiabatic time-dependent Hartree-Fock-Bogoliubov (ATDHFB) theory (Baran *et al.*, 2011).

The essence of this method is to assume that the generalized density matrix $\mathcal{R}$ evolves with time according to

$$\mathcal{R}(t) = e^{i\chi(t)}\mathcal{R}_0 e^{-i\chi(t)},$$

where $\chi(t)$ is a "momentum" coordinate conjugate to the generalized density matrix (Baranger and Veneroni, 1978). The adiabatic limit makes a Taylor expansion of this expression in χ, assuming terms beyond order χ^2 to be negligible. The collective inertia may be deduced by expanding the energy in terms of χ, collecting the kinetic energy as the quadratic terms. Through some steps reviewed in Appendix A, the collective inertia may be expressed in terms of the expansion of $\mathcal{R}$ and the collective coordinate q as (Baran *et al.*, 2011; Krieger and Goeke, 1974)

$$\mathcal{M} = \frac{i}{2\dot{q}^2}\mathrm{Tr}\left(\dot{\mathcal{R}}_0\left[\mathcal{R}_0, \mathcal{R}_1\right]\right).$$

The generator coordinate method (GCM) applied to fission dynamics incorporates the collective inertia calculated with ATDHFB. The GCM begins with a Hamiltonian operator in the collective degrees of freedom, which can be represented by

$$\hat{H}_{\text{coll.}} = -\frac{\hbar^2}{2}\sum_{ij}\frac{\partial}{\partial q_i}[(\mathcal{M}^{-1})]_{ij}\frac{\partial}{\partial q_j} + \overline{V}(q), \tag{2.13}$$

where $\mathcal{M}_{ij}$ is the collective inertia, the q_i are the collective coordinates, and $\overline{V}(q)$ is the collective potential corrected by the zero-point energy (Libert *et al.*, 1999; Yuldashbaeva *et al.*, 1999; Goutte *et al.*, 2005).

Effectively, the collective inertia in the perturbative, cranking approximation is calculated with the expression (Baran *et al.*, 2011)

$$\mathcal{M}_{ij} = \frac{1}{4}[M_{ij}^{(1)}]^{-1}M_{ij}^{(3)}[M_{ij}^{(1)}]^{-1} \tag{2.14}$$

(no summation over i or j intended), and the Gaussian-overlap approximation to the zero-point energy (Libert *et al.*, 1999) is

$$\mathrm{ZPE} = [M_{ij}^{(3)}]^{-1} M_{ij}^{(2)}.$$

The $M_{ij}^{(K)}$ are the moments

$$M_{ij}^{(K)} = \sum_{\alpha\beta} \frac{\langle 0|\, \hat{Q}_i \,|\alpha\beta\rangle \,\langle \alpha\beta|\, \hat{Q}_j^\dagger \,|0\rangle}{(E_\alpha + E_\beta)^K}, \tag{2.15}$$

where $\hat{Q}_i$ is the operator corresponding to a collective degree of freedom and $|\alpha\beta\rangle$ is a wave function involving two quasi-particles. This expression yields reasonable values for the collective inertia – spontaneous fission half-lives in the superheavy elements can be reproduced very accurately (Baran *et al.*, 2011). But the cranking inertia eliminates self-consistent feedback from time-odd terms, and it is impossible to directly generalize to finite temperature. While the time-odd terms are not expected to be very large, they will still carry a significant impact, and a complete analysis of their impact will be crucial (Hinohara *et al.*, 2012).

Another approach to the collective inertia, such as mean-field instantons (Negele, 1989; Skalski, 2008), may yield a route to the proper finite-temperature generalization.

2.5 Summary

We attempt to approach the problem of nuclear fission with the microscopic, self-consistent mean field theory. Our goal is to test the predictive power of this model – can a model of the nuclear interaction, determined by an energy density functional fit to data across the nuclear chart that excludes fission data, accurately predict quantities for fission such as barrier heights and spontaneous fission half-lives?

Testing the quality of a fission model is complicated on the one hand by static properties of the energy density functional itself, and on the other hand by the

assumptions of the dynamical model. It would be entirely possible to have an EDF that perfectly predicts fission isomeric energies and barrier heights, but for the dynamical model to be too restrictive. We look at the properties of static potential energy surfaces of ^{232}Th, ^{180}Hg, and across the actinide series to focus on the properties of the functional itself. We will then finally turn to look at the spontaneous fission half-lives predicted by the EDF coupled with collective inertias calculated self-consistently with ATDHFB.

Chapter 3

Third Minima in Thorium and Uranium

3.1 Introduction

The observables for a fissioning system, such as mass distribution and half-life, are sensitive to the sequence of nuclear configurations through which the nucleus is driven on the way to fission (Bjørnholm and Lynn, 1980). Isomeric states, which correspond to minima in the potential energy surface, represent metastable configurations which can be interesting to study in their own right. Superdeformed isomers, in which the ratio between the longest axis and the shorter axes is about 2:1, correspond to the second mininum in actinide nuclei and have been thoroughly studied since their discovery (see, e.g., Singh *et al.* (2002)). Continued studies of the actinides, especially ^{232}Th (Blons *et al.*, 1984; Blons, 1989) and ^{232}U (Csige *et al.*, 2009), inferred the existence of a highly elongated (with an axis ratio of 3:1) and reflection asymmetric isomer corresponding to a third minimum for these nuclei through analysis of resonances in the fission cross sections.

The hyperdeformed isomer corresponding to the third minimum is a reflection asymmetric configuration correlated closely with shell effects in the nascent fragments, with one fragment resembling the doubly-magic ^{132}Sn (Ćwiok *et al.*, 1994).

Past theoretical treatments of the thorium and uranium isotopes, especially those carried out with the macroscopic-microscopic model, have predicted third minima that agree well with those inferred through experiment. Self-consistent HFB studies (Bonneau *et al.*, 2004; Berger *et al.*, 1989), however, as well as a recent study with the macroscopic-microscopic model (Kowal and Skalski, 2012), typically find a third minimum that is much shallower than that of the liquid drop models or the empirical barrier fits. Is a third minimum truly necessary to reproduce experimental cross sections and spontaneous fission half-lives? If so, what physical effects are responsible for creating a deeper third minimum?

We calculate the two-dimensional potential energy surfaces of ^{232}Th and ^{232}U with the FT-DFT with the SkM* interaction, investigating how the potential energy surface and the third minima evolve with increasing excitation energy. As the excitation energy is increased and pairing is quenched, we actually find a regime in which the third minimum is slightly deepened for ^{232}Th. Because this result was unexpected, we also calculated the potential energy surfaces at corresponding excitation energies for ^{228}Th for comparison. These calculations are presented in Section 3.2. A further analysis of isotopic trends is presented in Section 3.3. We conclude our discussion of third minima in Section 3.4.

3.2 Potential Energy Surfaces

We present in Figs. 3.1 and 3.2 the surfaces of potential energy at constant entropy (which correspond to surfaces of free energy at constant temperature) for ^{232}Th at several excitation energies. As excitation energy increases from $E^* = 3.8$MeV to $E^* = 48$MeV, Fig. 3.1 shows that the second barrier actually shrinks and while a

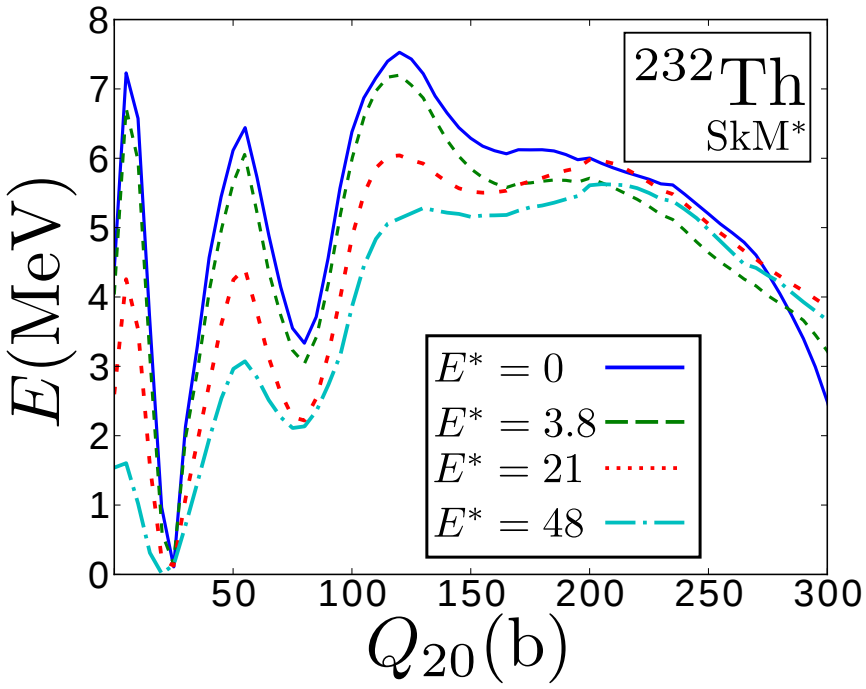


Figure 3.1: The one-dimensional potential energy curves at several excitation energies are plotted for ^{232}Th.

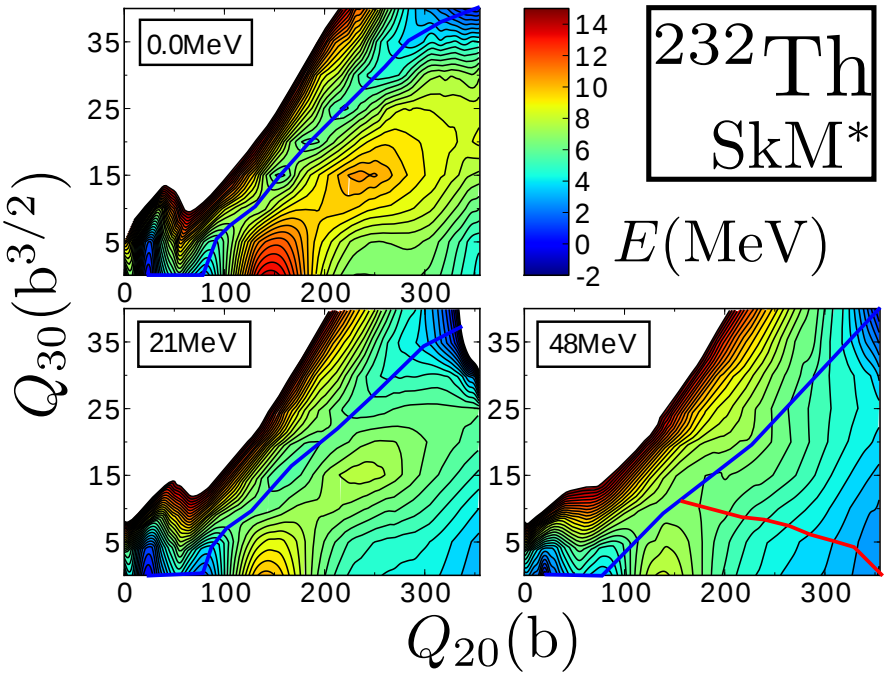


Figure 3.2: The potential energy surfaces at several excitation energies E^* are plotted for ^{232}Th. The lowest-energy pathway is traced in each plot. For $E^* = 48$MeV (lower right), the alternative, competing symmetric pathway is also traced.

third barrier maintains the height of the former plateau. This deepens the pocket where the expected third minimum appears.

At low excitation energies, the third minimum is barely seen in the HFB models. It is well known that pairing and shell effects oppose each other (Nazarewicz, 1993). As the excitation energy increases and pairing is quenched (as seen in Fig. 3.3), the underlying shell effects become stronger than the effects of pairing and the minimum becomes more pronounced.

In the vicinity of the third barrier, it is very interesting that the neutron pairing gap exhibits a hump where the proton gap exhibits a valley. This "mismatch" in phase may help to diagnose why SkM*, UNEDF1, and other HFB potential energy surfaces lack a dramatic third barrier.

Between $E^* \approx 21$MeV and $E^* \approx 48$MeV, the second and third barriers merge together so that the third minimum vanishes altogether. The potential energy surface

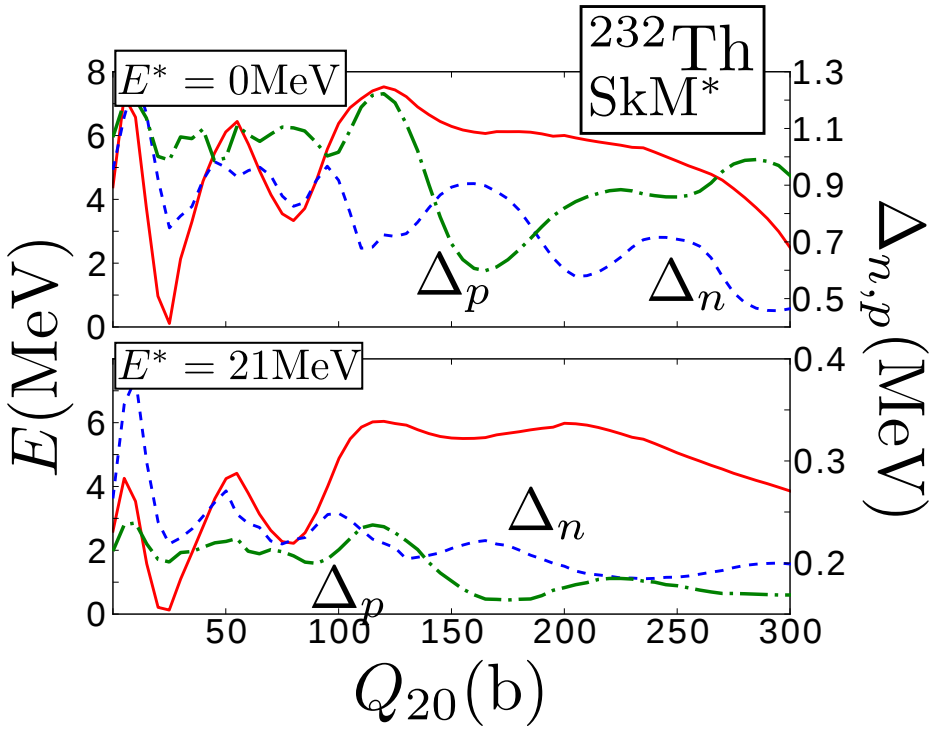


Figure 3.3: The free energy curves (red solid lines) at $E^* = 0$MeV and $E^* = 21$MeV are plotted for ^{232}Th, alongside the pairing gaps Δ_n and Δ_p (blue dashed line and green dot-dashed line, respectively).

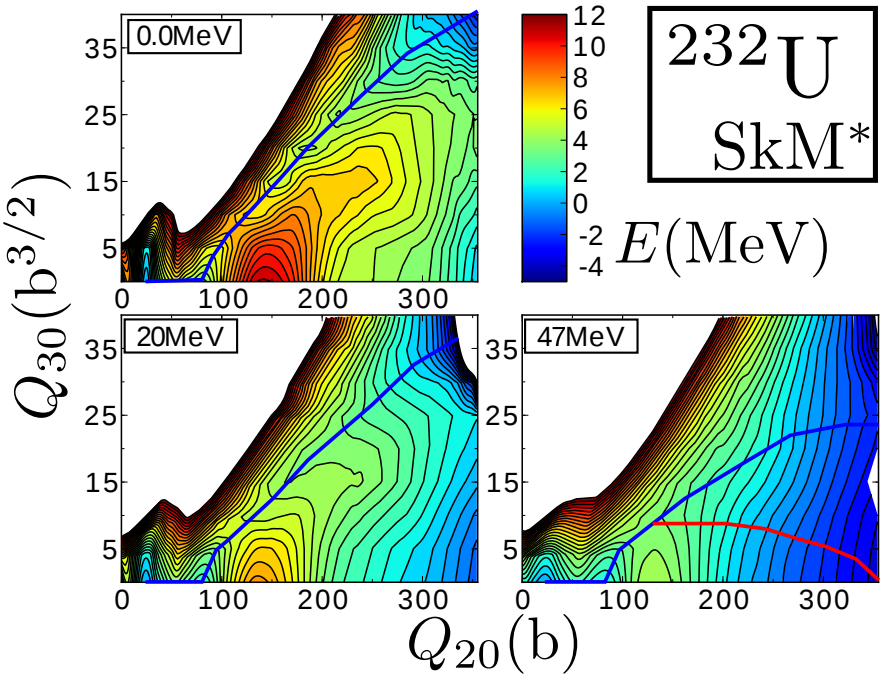


Figure 3.4: The potential energy surfaces at several values of E^* are plotted for ^{232}U.

for $E^* \approx 48$MeV also demonstrates that the pathway to symmetric fission is open, with the new symmetric fission barrier comparable in height to the second fission barrier in the $E^* = 0$MeV surface.

The experiment by Günther *et al.* (1980) measured the mass yield for the photofission of ^{232}Th, reporting that the ratio of symmetric yield to asymmetric yield increases from 2% to 10% for a Bremstrahlung energy range (corresponding approximately to our excitation energy) $E_{\text{B.S.}} = 15 - 55$MeV. It is encouraging that this FT-DFT study predicts the opening of the symmetric fission pathway in an energy range that is comparable to this experimental setup.

For ^{232}U, the potential energy surfaces at several values of E^* are shown in Fig. 3.4. The shallowness of the third barrier at $E^* = 0$ is similar to that of ^{232}Th. Similarly, the second and third barriers both shrink and merge together with increasing excitation energy, so that the barrier to the symmetric fission pathway falls rapidly to open the symmetric channel of fission.

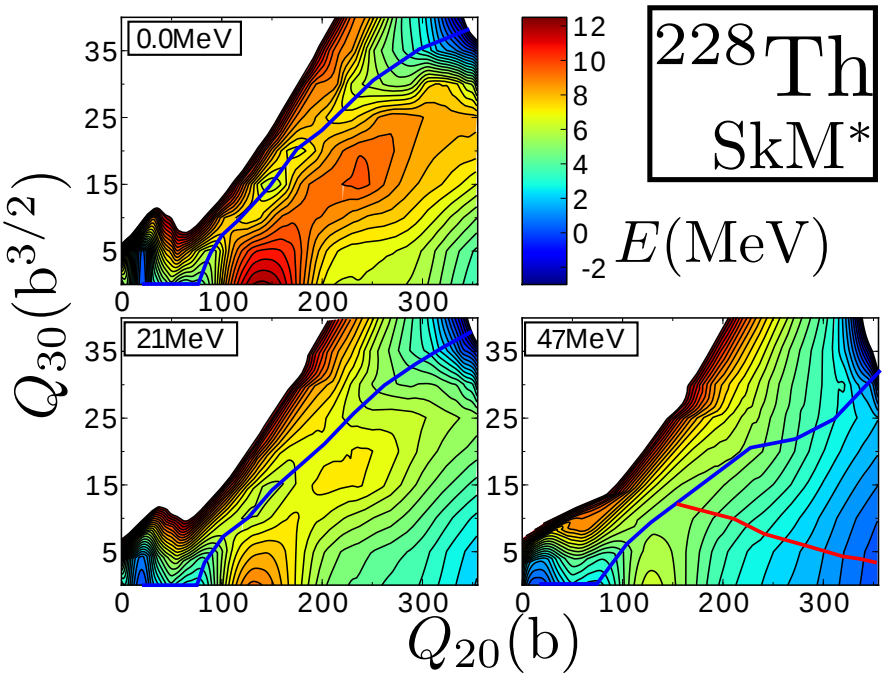


Figure 3.5: The potential energy surfaces at several excitation energies E^* are plotted for ^{228}Th.

The low excitation energy required for the appearance of the isomer/"shelf" is corroborated by the experiment of (Csige *et al.*, 2009) on ^{232}U. In our FT-DFT study, the very shallow third barrier for ^{232}U is seen to vanish quickly with increasing excitation energy.

Since the third minimum is almost nonexistent in the DFT studies of these two systems, we desired to study the evolution of a more substantial third minimum. A more complete survey of the actinides found more dramatic third barrier structures for isotopes such as ^{228}Th at $E^* = 0$MeV. We present the two-dimensional potential energy surfaces for ^{228}Th at several excitation energies in Fig. 3.5. The third minimum of ^{228}Th seems to slowly decrease up to an excitation energy of about $E^* \approx 21$MeV – by $E^* \approx 47$MeV, the minimum cannot be detected.

This HFB study qualitatively describes the situation seen in experiment mass yields, that the nucleus prefers more symmetric configurations as the excitation energy increases. For cases like ^{228}Th, in which the DFT calculation clearly delimits a third

minimum, the conditions that favor a hyperdeformed isomer dissolve quickly, and a symmetric fission pathway is opened up.

What are the microscopic physics that drive this evolution? In the next section, we turn to a systematic study of isotopic trends.

3.3 The Third Minimum through Isotopic Chains

DFT studies tend to predict either no third minimum or a very shallow one for ^{232}Th and ^{232}U. Macroscopic-microscopic studies tend to predict a rather deep third minimum, with the exception of (Kowal and Skalski, 2012). A more comprehensive survey of the actinides reveals that lighter isotopes of thorium and uranium do possess third minima even in DFT studies. What is the difference between isotopes that do possess a third minimum and those that do not? To answer this question, we calculate one-dimensional potential energy surfaces and shell correction energies at $E^* = 0$MeV.

The total shell correction energy $\delta E^{\text{sh.}}$ for thorium isotopes is presented in Fig. 3.6. The shell correction for $^{226-228}$Th demonstrates a clear maximum in the vicinity of the third barrier, as expected. This maximum becomes very shallow as neutron number increases. The third barrier can be identified readily in the SkM* curves for ^{226,228}Th, decreasing steadily with neutron number until the barrier is too shallow to detect for ^{232}Th. The potential energy curves for these four isotopes generated with the UNEDF1 functional show a similar steady lowering of the high-elongation region with increasing neutron number, but a clear third barrier can be identified only for ^{226,228}Th.

The neutron and proton shell corrections for several isotopes of Th are compared in Fig. 3.7. The proton shell correction energies show nearly identical trends in this isotopic chain, but the neutron shell corrections change depending on neutron number near the third barrier. The neutron shell correction energies of ^{226,228}Th maintain a hump through the region where the third barrier appears, whereas the neutron shell correction in ^{232}Th drops off sooner than the hump in ^{226,228}Th occurs.

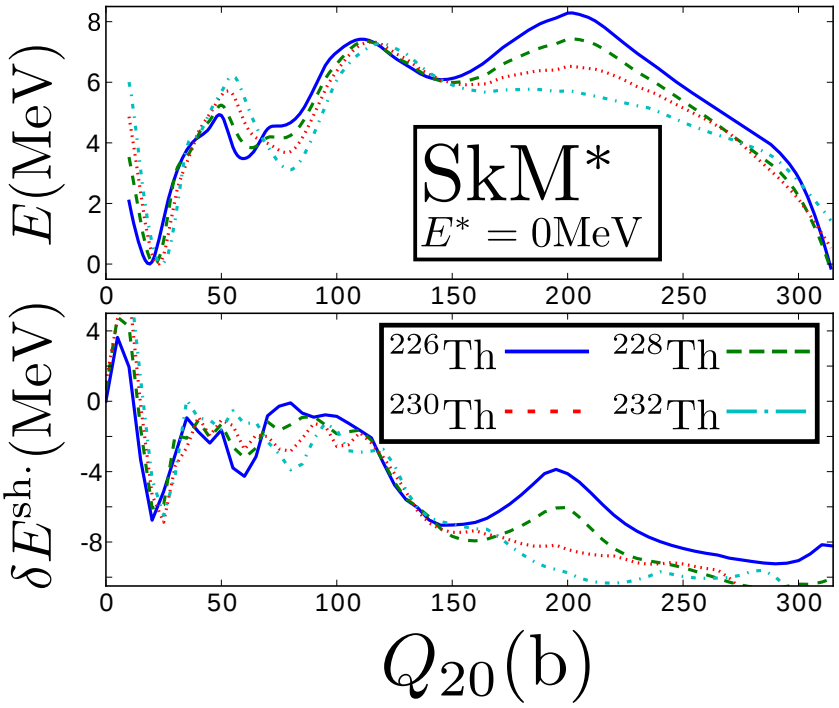


Figure 3.6: The potential energy curves (top) and total shell corrections $\delta E^{\rm sh.}$ (bottom) are plotted for $^{226-232}$Th at $E^* = 0$MeV.

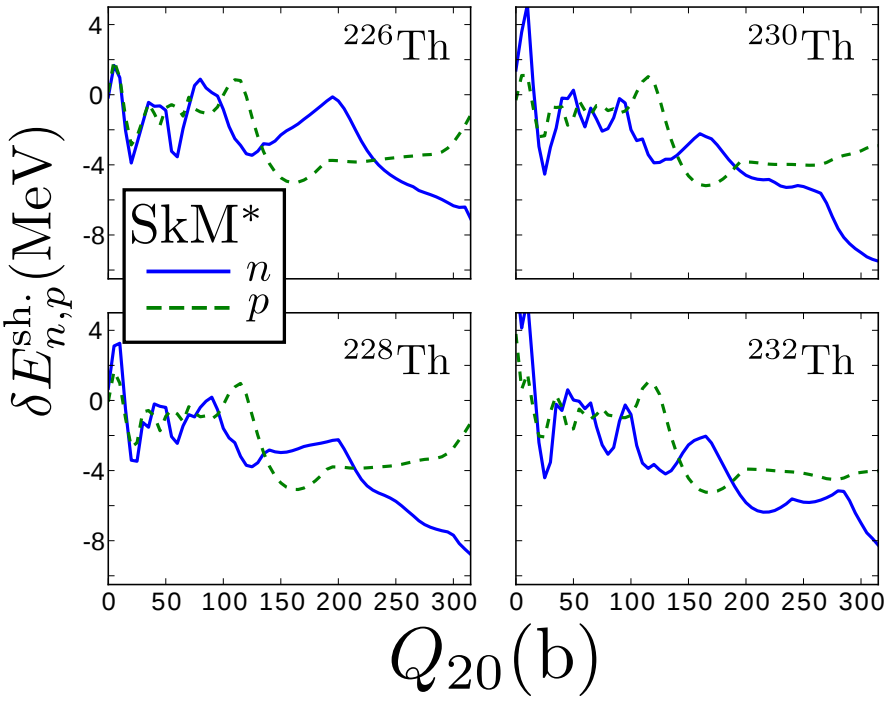


Figure 3.7: The neutron shell correction energy (blue lines) and proton shell correction energy (green dashed lines) are plotted for $^{226-232}$Th at $E^* = 0$MeV.

The shell correction energies for $^{226-232}$Th calculated with SkM* (see Figs. 3.6 and 3.7) and UNEDF1 (see Figs. 3.8 and 3.9) exhibit similar features, with a bump in the neutron shell correction where the third barrier is present. It is interesting that the neutron shell correction bump in the UNEDF1 calculation is consistently smaller than that obtained with SkM*.

For ^{232}Th, the third barrier is rather shallow in each of the DFT calculations seen in Fig. 3.10. The barrier is the shallowest in the UNEDF1 calculation – the potential energy curve has a negative slope in the third barrier region, rather than any clear plateau. As future UNEDF functionals are fit, it will be interesting to see whether this shell structure is robust, so that the third minimum remains shallower than that seen in other DFT studies, or whether the single particle effects might create a deeper third minimum.

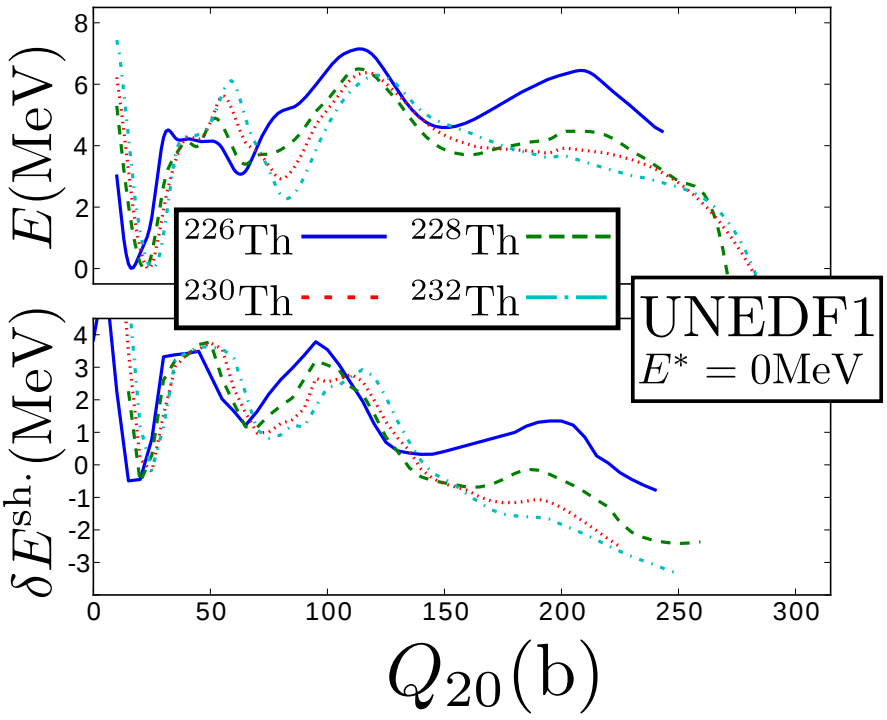


Figure 3.8: The potential energy curves (top) and total shell corrections $\delta E^{\mathrm{sh.}}$ (bottom), calculated with the UNEDF1 functional, are plotted for $^{226-232}$Th at $E^* = 0$MeV.

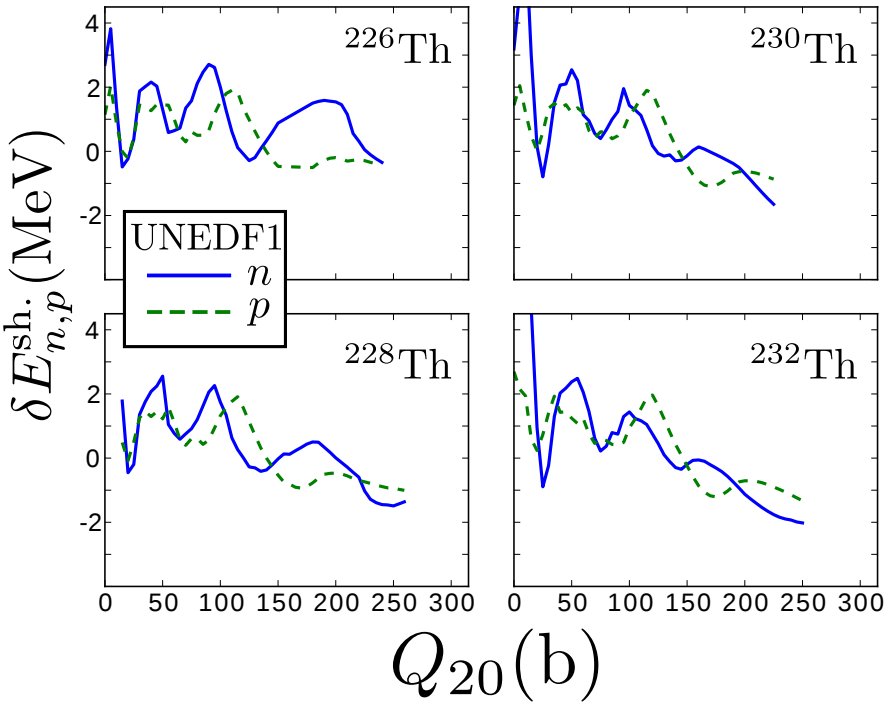


Figure 3.9: The neutron shell correction energy (blue lines) and proton shell correction energy (green dashed lines), calculated with UNEDF1, are plotted for $^{226-232}$Th at $E^* = 0$MeV.

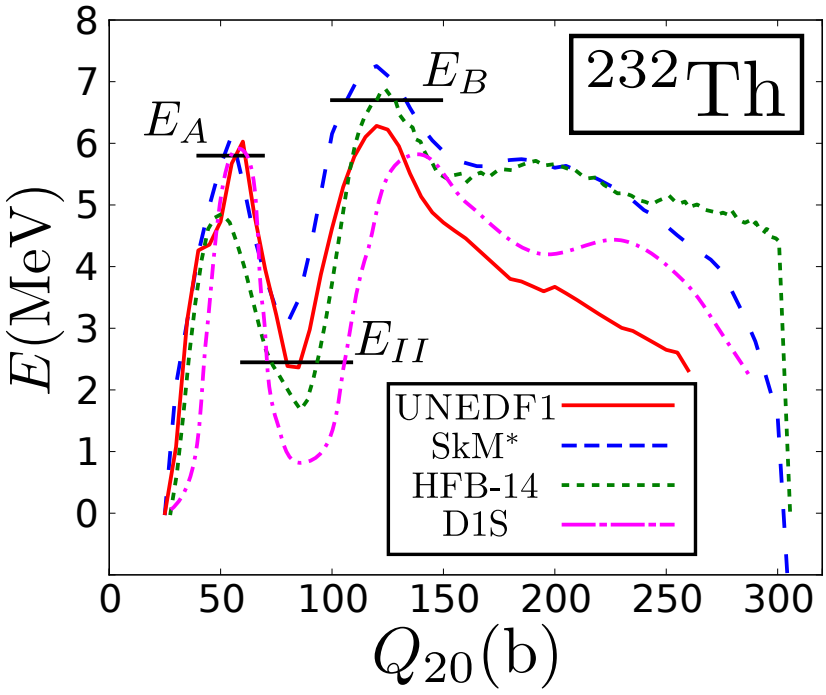


Figure 3.10: The free energy curves at $E^* = 0$MeV for ^{232}Th, using several parametrizations of the nuclear interaction. The empirically inferred values of the first and second barrier heights E_A and E_B (Capote *et al.*, 2009), as well as the second isomer E_{II} (Browne, 2006), are marked.

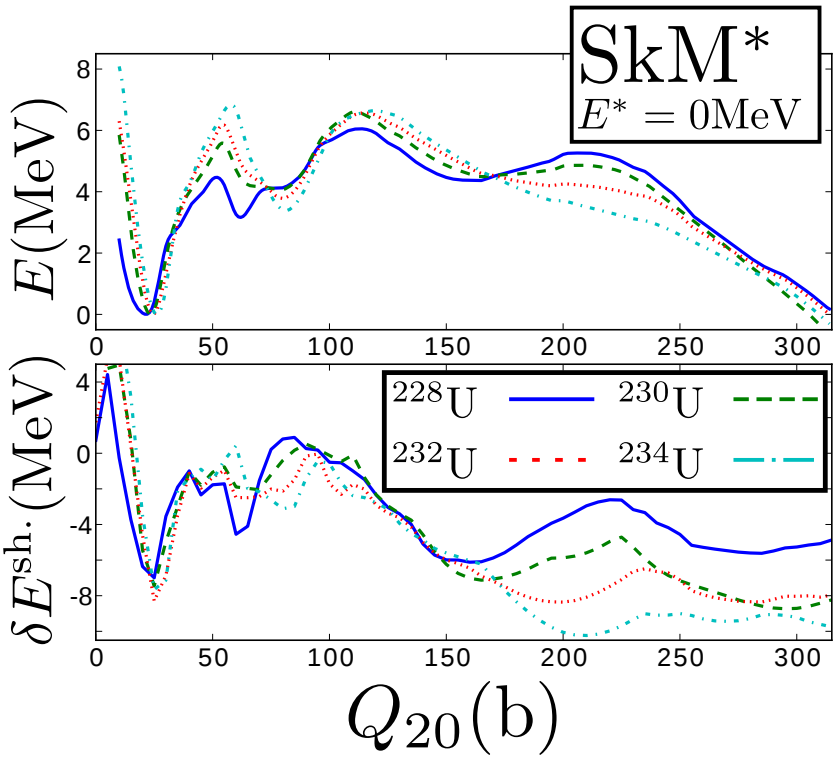


Figure 3.11: Same as Fig. 3.6, for $^{228-234}$U.

The total shell correction energy $\delta E^{\rm sh.}$ for uranium isotopes is presented in Fig. 3.11. The shell correction for ^{228}U demonstrates a clear maximum in the vicinity of the third barrier. As with the thorium isotopes, this maximum disappears as neutron number increases. And the proton and neutron shell corrections in Fig. 3.12 suggest similarly that the third barrier is driven by the neutron shell correction in the lighter isotopes.

The surfaces calculated with SkM*, at $E^* = 0.0$MeV, exhibit a less dramatic structure than that indicated in the experimental fits and the liquid drop model. While it is possible to locate the third minimum, it is much more shallow than the other sources would suggest. Past studies have attributed the almost equal splitting of the second barrier to shell effects; perhaps the shell effects present in SkM*, UNEDF1, and other DFT models are not strong enough to cause the splitting to the same degree.

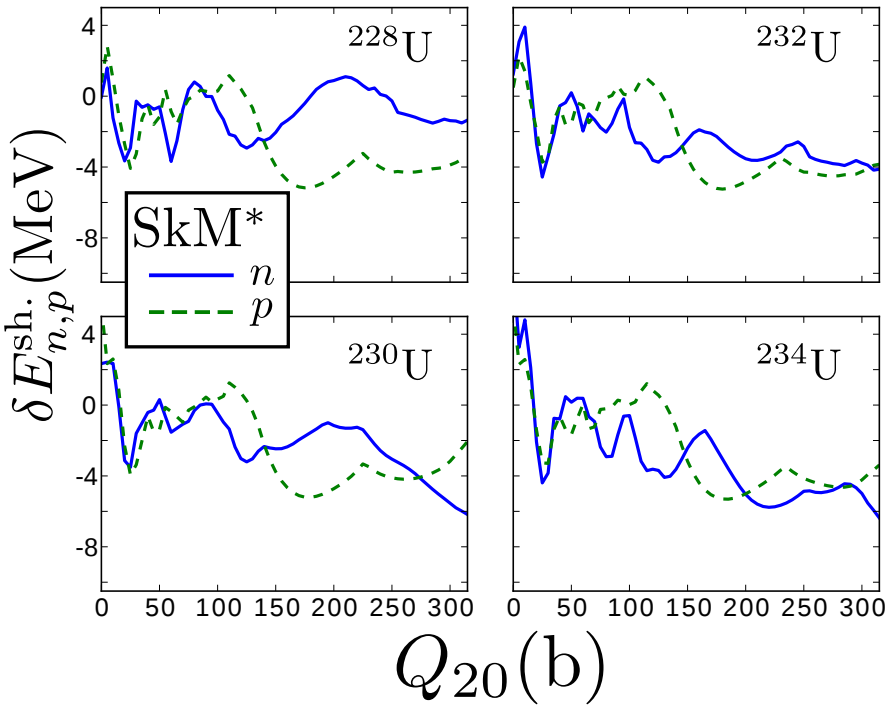


Figure 3.12: Same as Fig. 3.7, for $^{228-234}$U.

3.4 Conclusions

This study demonstrates that FT-DFT with Skyrme functionals locates very shallow third minima in the potential energy surfaces for ^{232}Th and ^{232}U. For systems in which a clear minimum is present, such as the prediction for ^{228}Th with SkM*, the minimum is found to be quite sensitive to excitation energy, so that the conditions needed for the hyperdeformed isomer to exist are washed out as the symmetric fission channel is opened.

The shallowness of the third minimum for ^{232}Th and ^{232}U is a robust feature of DFT calculations, consistent for such functionals as SkM*, UNEDF1, and D1S. DFT studies do, however, predict clear third minima for isotopes with fewer neutrons, such as ^{226,228}Th and ^{228}U. This sensitivity to the neutron shell effects is interesting.

The inference of a hyperdeformed fission isomer from experimental data does rely on several assumptions of the fission model. While microscopic, self-consistent

calculations generally predict a shallow or non-existent third minimum for ^{232}Th and ^{232}U, it is impossible to glean an alternative explanation of the experimental data from static calculations. The work by Mirea and Tassan-Got (2009) suggests that an explanation of the data lies in the dynamics of the fission process in the rearrangement of single-particle levels – it is tantalizing to consider what fully dynamic, microscopic, self-consistent calculations will uncover. Indeed, even though the total potential energy surfaces do not present clear minima, individual single particle levels may exhibit minima on which the resonances observed in experimental cross sections are built (Nazarewicz, 1993, see Section 7.1 and 7.3 for similar situations in Pb and Pt).

In light of new macroscopic-microscopic model calculations, it appears that this picture of a shallow, broad region of the PES where the third minimum was previously identified may be an accurate physical picture. Such a "shelf" may still produce the resonances observed in experiment, and this hypothesis must be followed up with further study.

Chapter 4

Study of the Asymmetric Fission of ^{180}Hg

4.1 Introduction

The very recent experimental discovery of asymmetric fission in ^{180}Hg (via β-delayed fission from ^{180}Tl) came as a surprise (Andreyev *et al.*, 2010). As fission fragmentation in the actinides are often determined by the shell effects of the fragments themselves, logic would lead to the conclusion that the most likely division is into two ^{90}Zr nuclei, due to semi-magicity. The experiment observed a more likely split of ^{100}Rb and ^{80}Kr, neither of which is near magicity. What drives this system to asymmetric fission if not (obvious) shell effects in the fragment nuclei?

A theoretical description of this system via the macroscopic-microscopic method has been put forward (Andreyev *et al.*, 2010; Möller *et al.*, 2012b; Ichikawa *et al.*, 2012), and this system has been recently visited by a self-consistent microscopic study by Warda *et al.* (2012). Both theoretical treatments consider only the nucleus at zero temperature. But all experiments that study the fission of mercury occur at a non-zero excitation energy – the electron capture considered by Andreyev *et al.* (2010) produced ^{180}Hg with up to 10.44MeV of excitation energy. Therefore, we consider the

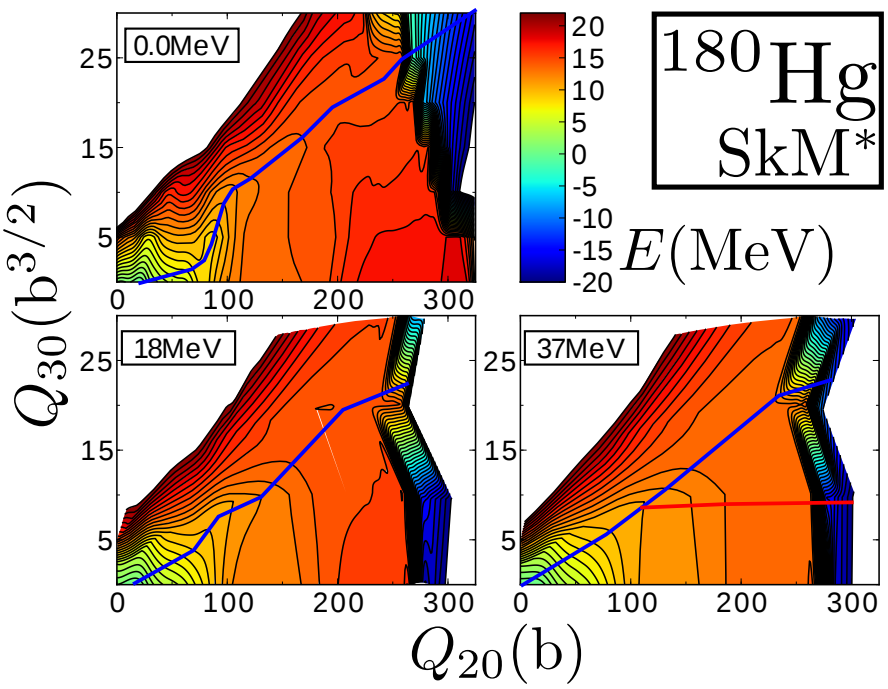


Figure 4.1: The potential energy surfaces for ^{180}Hg at several values ofE^*. The contour lines are separated by 1 MeV.

fission of the mercury isotopes with FT-DFT, studying the evolution of the symmetry of the nucleus in the scission region with increasing excitation energy. We explore the similarities and differences between ^{180}Hg and ^{198}Hg, as well as comparisons between the mercury isotopes and our study of the thorium and uranium isotopes.

4.2 Results

For the actinides, it is well known that mass yields tend to be asymmetric at low excitation energy, and that the symmetry of the mass yield increases with increasing excitation energy. Does the same hold true for ^{180}Hg? We choose representative excitation energies to demonstrate the evolution of the potential energy surface of ^{180}Hg with excitation energy. The surface for $kT = 1.0$ MeV, corresponding to $E^* \approx 18$ MeV, is shown in the lower left panel of Fig. 4.1. This excitation energy corresponds approximately to the collapse of pairing, where actinides begin to favor

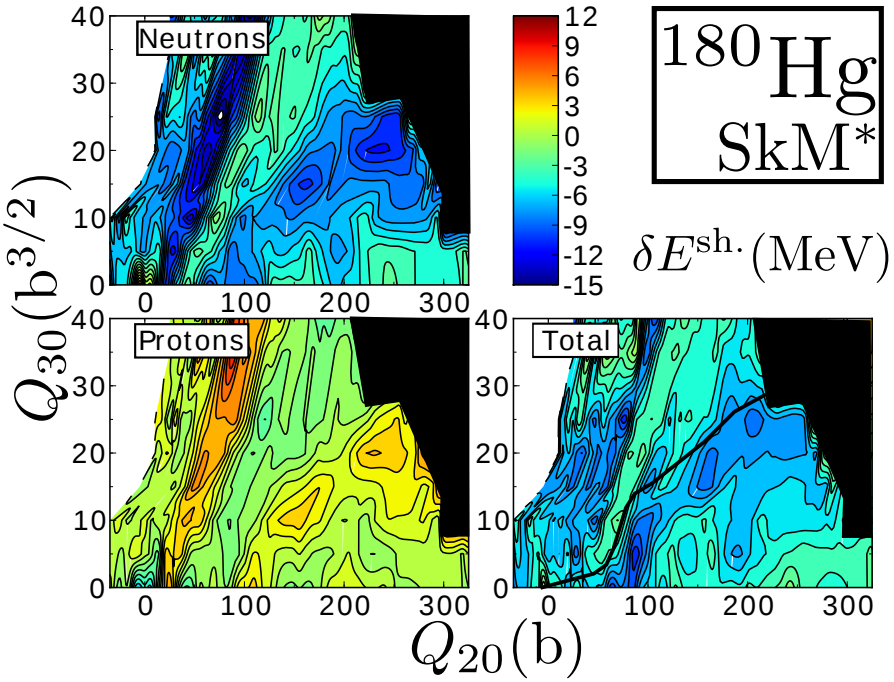


Figure 4.2: The shell correction energies for ^{180}Hg. The contour lines are separated by 1 MeV. The region beyond where scission occurs is black.

less asymmetric shapes. For ^{180}Hg at this excitation energy, the fission path still demonstrates a preference for asymmetric configurations – the symmetric pathway is impeded by a barrier about 1MeV higher than the asymmetric pathway. The barrier to the symmetric pathway, however, is substantially lowered relative to that for the $E^* = 0$MeV case.

The potential energy surface of ^{180}Hg for $kT = 1.5$ MeV, corresponding to $E^* \approx 37$ MeV, is shown in the bottom right panel of Fig. 4.1. The fission barrier in the symmetric pathway is lowered considerably, and it competes with the asymmetric pathway. Whether the symmetric or asymmetric pathway is favored would be determined decisively with a finite temperature calculation of the system's collective inertia. Indeed, the finite temperature collective inertia would allow a much more precise determination of the excitation energy where the transition from asymmetric to symmetric fission modes occurs.

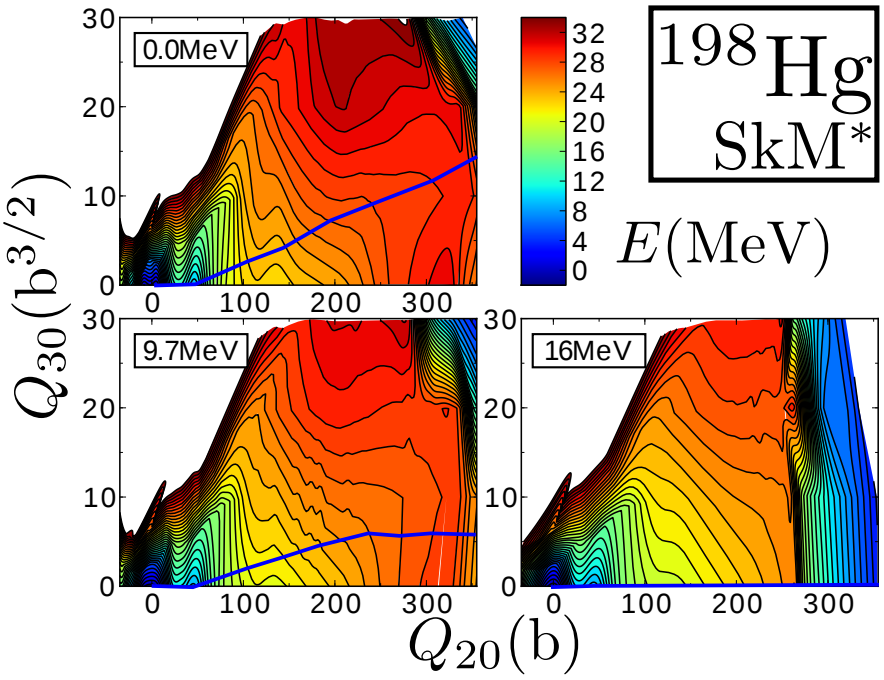


Figure 4.3: The potential energy surface for ^{198}Hg at various values of E^*. The contour lines are separated by 1 MeV.

The shell correction energies for ^{180}Hg are presented in Fig. 4.2. In the scission region, the total shell correction energies have a significant drop that drives the nucleus to favor an asymmetric fission pathway. The asymmetric pathway is favorable over the symmetric pathway by nearly 10MeV.

For ^{198}Hg (Fig. 4.3), the asymmetric fission pathway, which reaches smaller values of Q_{30} than that for ^{180}Hg, is dominant up to about $E^* \approx 9.7$MeV, where pairing is approaching zero. By $E^* \approx 15.7$MeV, the potential energy surface prefers a symmetric pathway, with a large barrier forcing the system away from the asymmetric pathway. This changeover to the symmetric fission mode is faster than that seen for the thorium and uranium nuclides.

The shell correction energies for ^{198}Hg are presented in Fig. 4.4. While the total shell correction energies in ^{180}Hg clearly favored the asymmetric pathway to scission, the shell correction energies in ^{198}Hg favor the less-asymmetric pathway, presenting a substantial barrier to greater asymmetry.

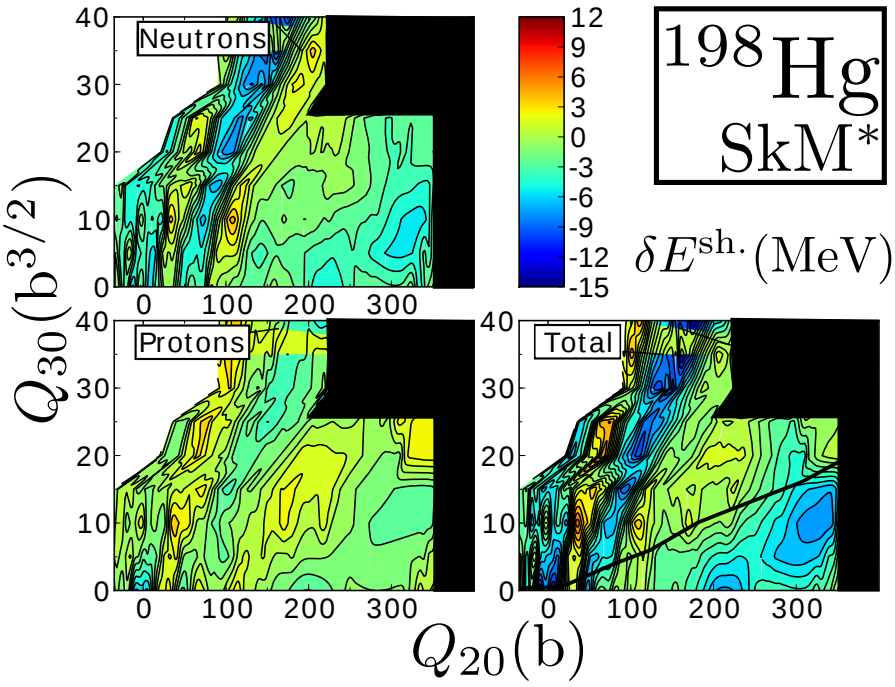


Figure 4.4: Same as Fig. 4.2, for ^{198}Hg.

Since the fragmentation of ^{180}Hg was experimentally observed to be asymmetric, rather than the symmetric fragmentation that might be expected due to the semi-magicity of ^{90}Zr, it is rewarding to see that the fission pathway follows the trends in the shell correction energies.

4.3 Conclusions

For the first time, the fission of mercury isotopes is studied with FT-DFT, exploring the evolution of the symmetry of fission products with increasing excitation energy. This is a valuable step towards a theoretical description of the recent experimental phenomenon of asymmetric fission in neutron-deficient preactinides.

Our potential energy surfaces with the SkM* functional demonstrate the proclivity of ^{180}Hg towards an asymmetric fission pathway when the nucleus has low excitation energy. As excitation energy is increased, we see a gradual lowering of the barrier

to the symmetric fission pathway, so that symmetric fission dominates at still higher excitation energies. This is consistent with the picture of fission in the major actinides.

The potential energy surface of ^{198}Hg, with only a slight preference for asymmetry at $E^* = 0$MeV, responds to increasing excitation energy in a manner similar to the actinides, such as ^{232}Th and ^{232}U – the potential energy surface demonstrably prefers a symmetric fission path when the excitation energy is increased.

While all mercury isotopes were once thought to fission symmetrically, the theoretical picture indicates that the symmetric fission mode is indeed open at the high excitation values typically available in experiments. Lower excitation energies allow the study of shell effects as they evolve across the mercury isotopes. That the lighter isotope (^{180}Hg) demonstrates the clearest preference for asymmetric fission for a significant range of excitation energies is reminiscient of the lighter thorium and uranium isotopes possessing a deeper third minimum (with reflection-asymmetric isomer) than heavier isotopes. That is, in both cases the shell effects that drive a special, asymmetric structure are strongest in the lightest isotopes.

The success in capturing these salient features with this microscopic, self-consistent fission model, whose only phenomenological input is the nuclear force parametrization, is highly encouraging.

Chapter 5

Survey of Spontaneous Fission in the Actinides

5.1 Introduction

As superheavy elements are being discovered and as r-process nuclei are being probed, it is important to benchmark our theories of the nuclear interaction in regions in the nuclear chart where data are very well known. We evaluate the performance of the new UNEDF1 functional of Kortelainen *et al.* (2012) in describing the nuclear potential energy surface needed for fission studies.

In light of a recent study with covariant density functional theory, we investigate whether triaxiality plays a significant role near the *second* fission barrier in Section 5.2. We then turn to the survey of actinide fission barrier heights and isomeric energies in Section 5.3. We evaluate the half-lives predicted by UNEDF1 and SkM* in Section 5.4, and conclude our survey of actinide fission properties in Section 5.5.

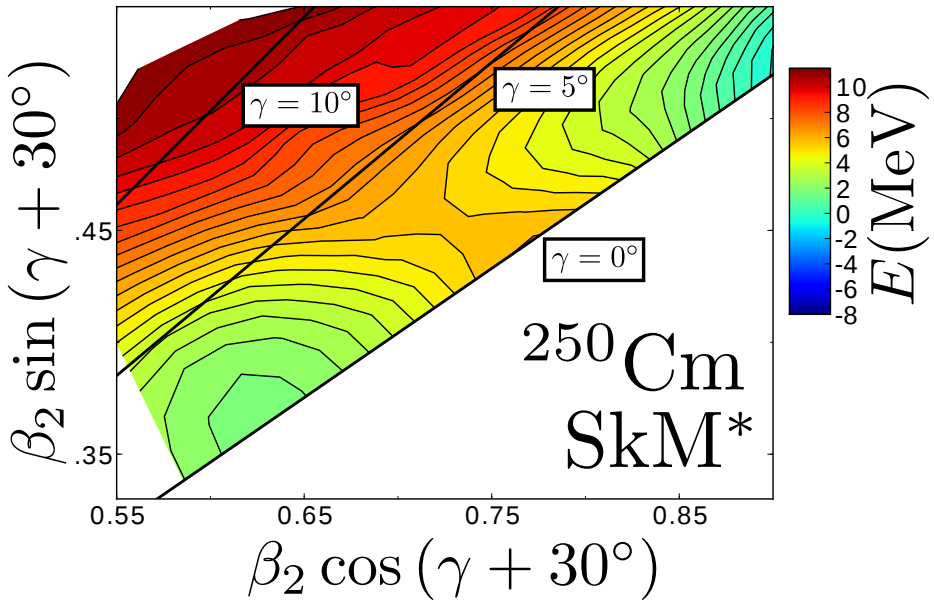


Figure 5.1: The potential energy surface of ^{250}Cm, calculated with SkM*, is plotted in (β, γ) coordinates, in the vicinity of the second barrier. The contour lines are separated by 0.5MeV.

5.2 Triaxiality at Second Barrier

A recent study by Lu *et al.* (2012) using covariant density functional theory asserted that triaxiality can lower the height of the *second* fission barrier – triaxiality is well-known to lower the first fission barrier, while it was previously thought to play no role beyond the first barrier. The second barrier is certainly lowered by reflection asymmetric configurations, so an additional lowering due to broken axial symmetry would be a surprise. Since we want the most accurate survey of fission barrier heights possible, we examine the effect of the triaxial degree of freedom on the *second* fission barrier for ^{250}Cm (where Lu *et al.* (2012) reported the most dramatic triaxial effect).

For ^{250}Cm (Figs. 5.1 and 5.2), a meander into triaxial shapes near the *second* barrier appears to lower the second barrier substantially, by nearly 1MeV. For a triaxial measure of $\gamma \approx 2.5°$, this is a surprisingly large gain in energy. Checking

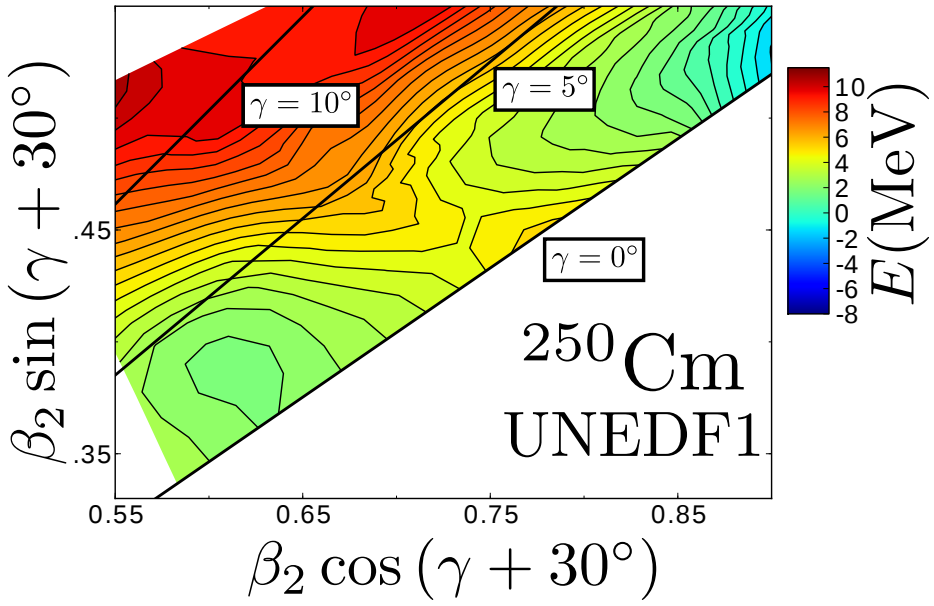


Figure 5.2: Same as Fig. 5.1, calculated with the UNEDF1 functional.

this result with SkM*, the wander into triaxiality apparently remains – the difference between the axial barrier height and the triaxial saddle point height is about 500keV.

The second minimum also displays triaxial softness for UNEDF1, but not for SkM*.

We explore the shell corrections for ^{250}Cm in Figs. 5.3 and 5.4, attempting to understand why triaxiality might be favorable near the second barrier. It appears that both protons and neutrons produce a maximally positive shell correction in the vicinity of the second barrier, so that a meander into triaxiality relaxes the system.

In light of this small but non-zero effect of triaxiality on the height of the second barrier, we continue our survey of the actinides with calculations in which axial symmetry is allowed to be broken. Indeed, the effect of triaxiality on the second barrier is negligible in most cases, but releasing this symmetry restriction is valuable for exploring the full array of configurations through which the nucleus travels on its way to fission.

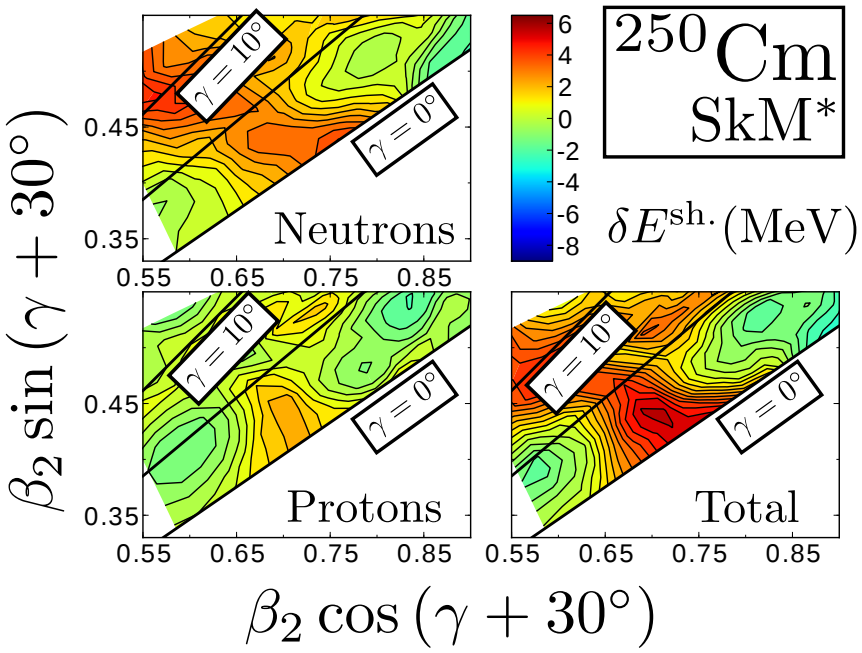


Figure 5.3: The neutron, proton, and total shell correction energies $\delta E^{\text{sh.}}$ for ^{250}Cm, calculated with SkM*.

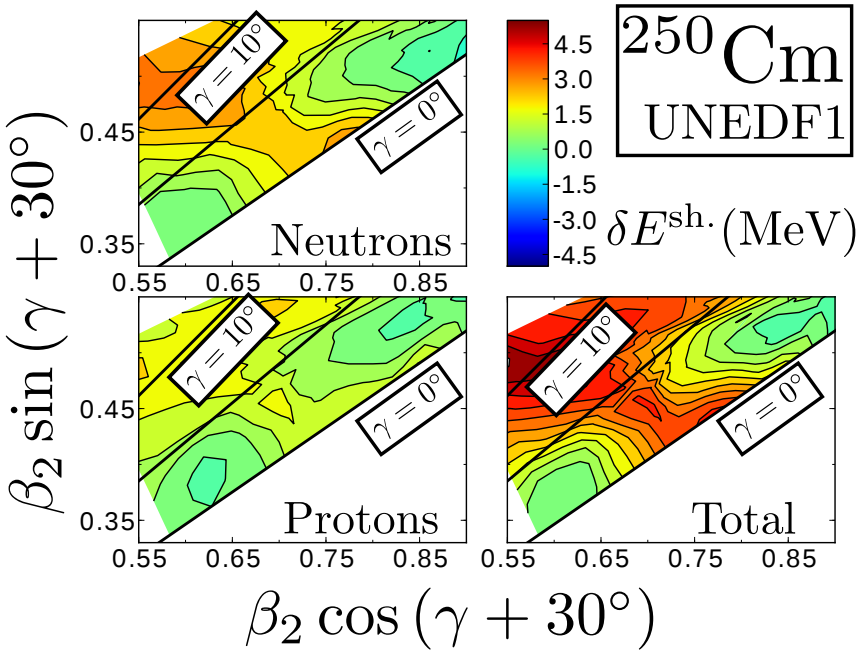


Figure 5.4: Same as Fig. 5.3, calculated with the UNEDF1 functional.

5.3 Systematic Fission Barrier Heights

While the fission barrier height is not directly observable, the empirical barrier heights (inferred from induced fission probability measurements) do provide an important constraint on theory. If a theory were to predict the exact same barrier heights as have been deduced empirically, the theory would also reproduce the real fission probability under the same assumptions for optical parameters.

We compare the predictions of UNEDF1, SkM*, D1S (Delaroche *et al.*, 2006), and the microscopic-macroscopic FRLDM (Möller *et al.*, 2009) models for the inner fission barrier height (Fig. 5.5; residuals in Fig. 5.6), the energy of the superdeformed fission isomer (Fig. 5.7; residuals in Fig. 5.8), and the second barrier height (Fig. 5.9; residuals in Fig. 5.10) with empirical values (Capote *et al.*, 2009; Smirenkin, 1993). The residuals are calculated as the theoretical prediction subtracted from the experimental quantity.

The UNEDF1 and SkM* functionals tend to overestimate the inner fission barriers, especially for U and Pu.

For the isomeric energies, the three self-consistent calculations considered here perform similarly. This is consistent with the ease with which HFB finds local minima, and the difficulty with which HFB finds local saddle points. UNEDF1 reproduces isomeric energies beyond the four nuclei to which it was fit – this strengthens the case for the predictive power of UNEDF1.

For the outer barrier heights, UNEDF1 reproduces empirical barrier heights as accurately as or more accurately than the other forces considered. The Pu and Cm chains reveal a curvature to the isotopic trend that is too strong – the empirical barrier heights are nearly constant for both elements, while UNEDF1 predicts a clear peak at $N = 150$ for Pu and $N = 152$ for Cm. But this curvature remains less severe than, e.g., that seen in the D1S trends.

On comparison with empirical fission barrier heights and isomer energies, the performance of UNEDF1 is on par with that of the other self-consistent interactions

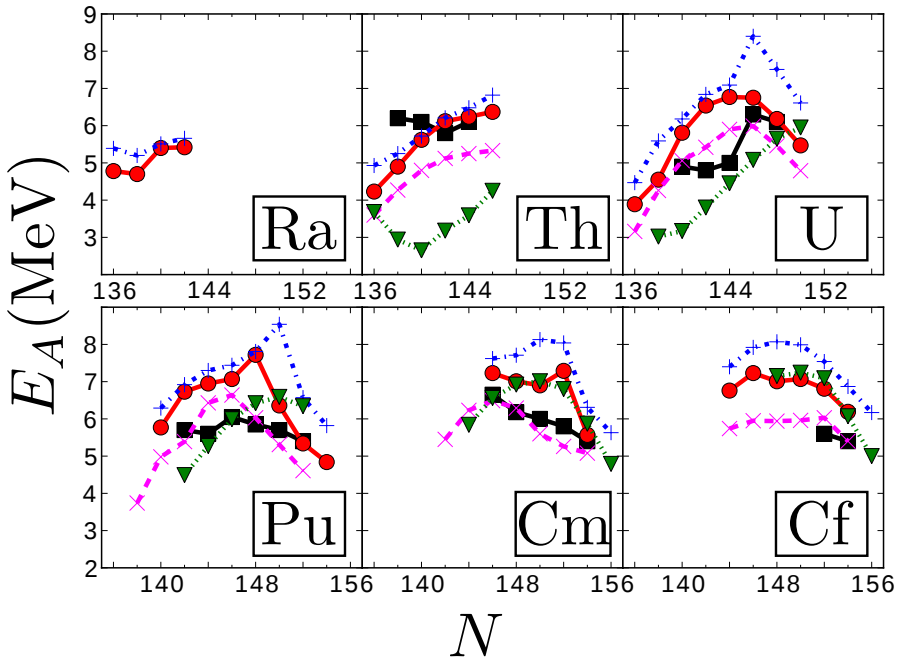


Figure 5.5: The inner barriers of several actinide nuclides are plotted. The black lines with square markers represent experimental data (Capote *et al.*, 2009; Smirenkin, 1993); the red lines with circles are the predictions of UNEDF1; the blue lines with plus signs are SkM*; the magenta lines with 'x'-es are D1S (Delaroche *et al.*, 2006); and the green lines with triangles are the predictions of the FRLDM model (Möller *et al.*, 2009).

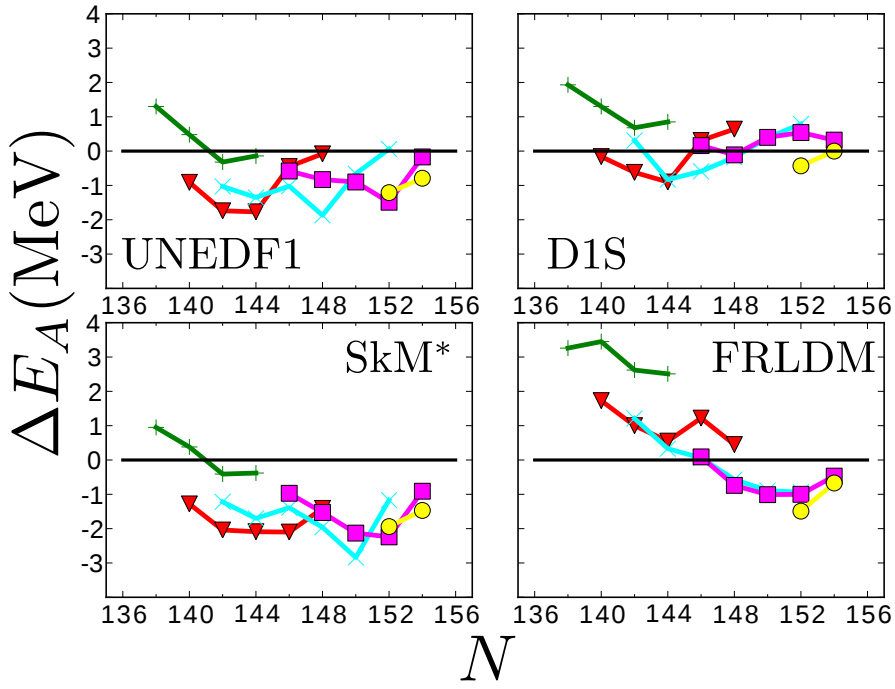


Figure 5.6: The residuals for the inner barriers of several actinide nuclides are plotted. The green lines with plus signs are Th isotopes; red lines with inverted trianges are U; cyan lines with 'x'-es are Pu; magenta lines with squares are Cm; and yellow lines with circles are Cf.

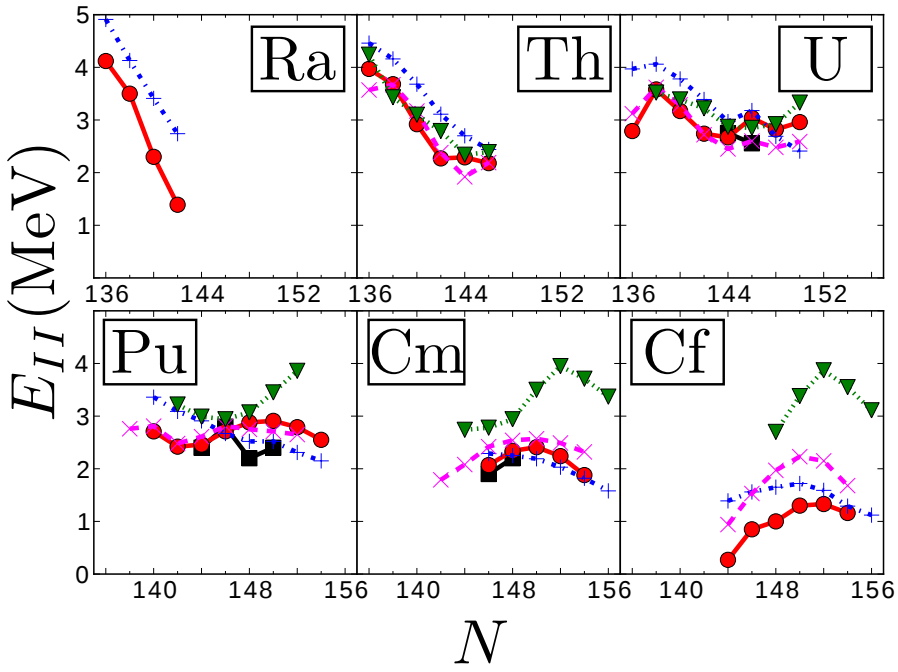


Figure 5.7: The energies of the fission isomers for the actinide nuclides, with the same legend as Fig. 5.5. The experimental data are from Singh *et al.* (2002).

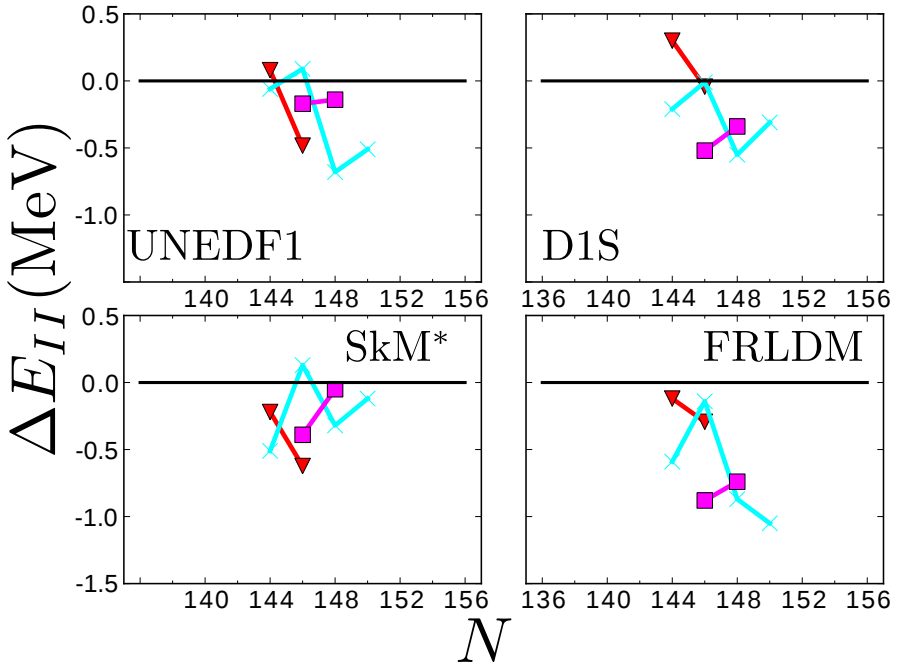


Figure 5.8: Same as Fig. 5.6, for isomeric energies.

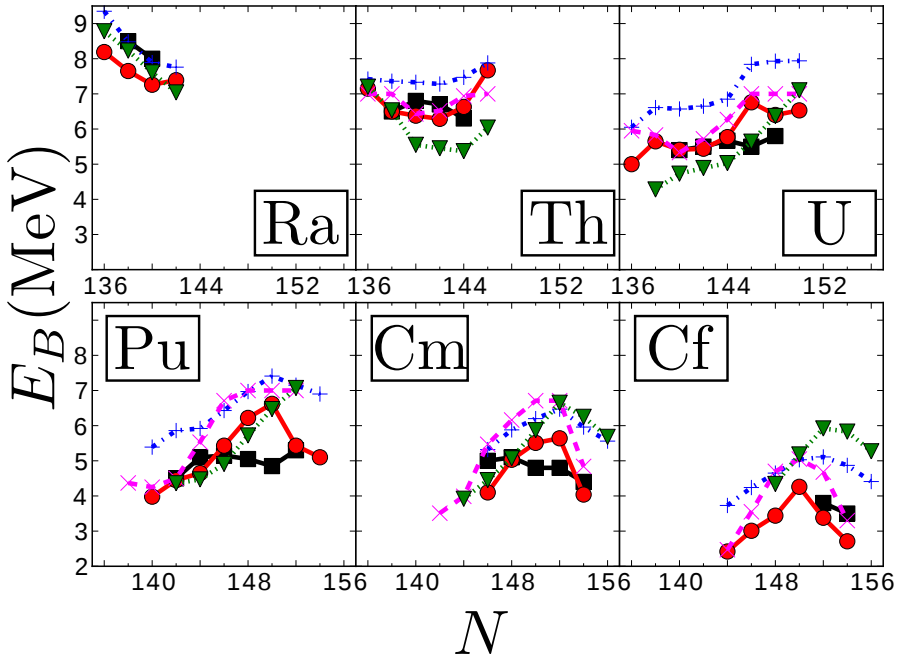


Figure 5.9: The outer barriers of several actinide nuclides, with the same legend as Fig. 5.5.

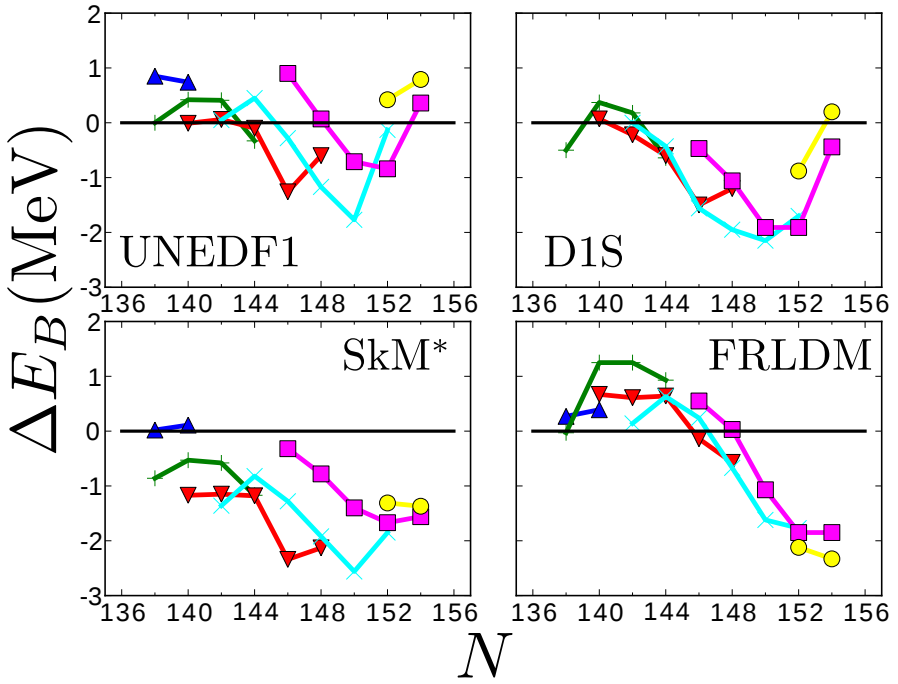


Figure 5.10: Same as Fig. 5.6, for outer barrier heights. The additional blue lines with triangles are Ra isotopes.

Table 5.1: For each theoretical model, the RMS deviations of the first barrier height E_A, the fission isomer E_{II}, and the second barrier height E_B are given for the selection of even-even nuclei considered.

	UNEDF1	FRLDM	SkM*	D1S
E_A	1.03	1.52	1.61	0.709
E_{II}	0.357	0.675	0.351	0.339
E_B	0.690	1.13	1.39	1.14

and the macroscopic-microscopic FRLDM. Table 5.1 displays the RMS deviations of the four theoretical models in the nuclides considered here, relative to empirical values. The D1S functional yields the best agreement (with an RMS of 0.709MeV) for inner barrier heights, but UNEDF1 agrees nearly as well (with an RMS of 1.03MeV). The three self-consistent calculations (UNEDF1, SkM*, and D1S) yield similar levels of agreement for the fission isomer energy – this is consistent with the ease with which self-consistent calculations locate minima. For the outer barrier heights, UNEDF1 yields the best agreement with empirical values, with an RMS of 0.690MeV. The FRLDM and D1S predictions for outer barrier heights have a similar level of agreement (RMS values of 1.13MeV and 1.14MeV, respectively).

While UNEDF1 was fit to data including four superdeformed isomers, the functional was not readjusted to fission-specific data. The ability of UNEDF1 to reproduce empirical barrier heights and isomer energies and their trends across the actinide series presents a strong case for its predictive power.

5.4 Systematics of Spontaneous-Fission Half-lives

The calculation of the half-life requires realistic values for the collective inertia and for the zero-point vibrational energy. The best values for these quantities are currently obtained with the adiabatic time-dependent HFB (ATDHFB) in the perturbative-cranking limit (Baran *et al.*, 2009).

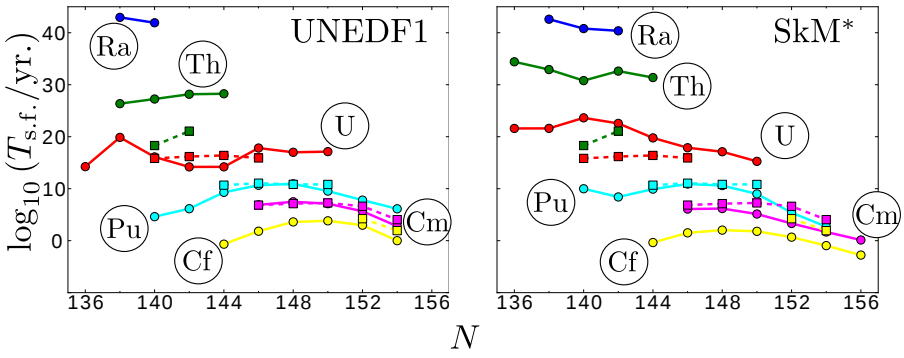


Figure 5.11: The logorithm of spontaneous fission half-lives are plotted. Experimental values (Holden and Hoffman, 2000) are plotted with squares, and the predictions of UNEDF1 (left panel) and SkM* (right panel) are plotted with circles. Isotopic chains are labeled by element name.

Because the pairing values produced by UNEDF1 are too small in the actinide region, the resulting collective inertia parameters are too large. The inertia parameters also incorporate only time-even terms: any information coming from time-odd feedback is lost. As such, the inertias were adjusted by a multiplicative factor chosen to adjust the half-life of ^{240}Pu to the experimental one. This simple adjustment produces remarkably good results across the actinides, as can be seen in Fig. 5.11 – it would have been undesirable to require an adjustment for each isotopic chain, as such a refitting would degrade the predictablility of our model.

For isotopic chains with $Z \geq 94$, the theoretical predictions for the trends in half-lives agree well with the experimental trends where data exist, lending confidence to the predictions where data are not known. The half-lives for the thorium chain seem to be consistently overestimated. The half-lives for a few radium isotopes are plotted as predictions.

The general agreement seen in the isotopic trends predicted by both UNEDF1 and SkM* indicate the importance of both accurate barrier height predictions and accurate accounting of the fission dynamics. It will be interesting to see what effect time-odd terms in the collective inertia will have on the spontaneous fission half-life.

Since the experimental data span nearly twenty orders of magnitude (from the short half-life of ^{252}Cf to the long half-life of ^{232}Th), the agreement between the predicted trends and the experimental trends is quite impressive, well in line with the systemmatics seen in studies of the super-heavy elements.

5.5 Conclusions

This systematic comparison of the UNEDF1 fission barriers with those of experiment as well as other theoretical approaches shows that the UNEDF1 functional is competitive with the best approaches to fission.

In light of the recent study by Lu *et al.* (2012), we evaluated whether triaxiality would have a significant effect on the second barrier heights in the actinides. We found the largest effect in ^{250}Cm, where the UNEDF1 calculation predicts a lowering of about 1MeV and the SkM* calculation predicts a lowering of about 0.5MeV. Because the lowering was so large for such a small degree of triaxiality, we examined the shell correction energies, which reveal that, indeed, there is some change in configuration that drives the system to break axial symmetry, even if only to a small degree.

For the global survey of actinide fission barrier heights, isomer energies, and spontaneous fission half-lives, we found that the new UNEDF1 functional yields predictions that agree with experimental values as well as or better than other approaches. It is valuable to see that several microscopic approaches to fission produce fission barrier predictions of a quality similar to macroscopic-microscopic approaches. The spontaneous fission half-lives predicted using the SkM* functional and the UNEDF1 functional are in excellent agreement with experimental values. Since no fission data were incorporated into the fit for UNEDF1, this represents a significant step towards a truly predictive, microscopic theory of fission.

Chapter 6

Conclusion

We have explored the implications of a theory of fission based on a self-consistent, microscopic DFT. We have studied ^{232}Th and ^{232}U, systems in which phenomenological methods expect hyperdeformed isomers to exist. We then turned to a study of the surprising properties of the fission of ^{180}Hg and ^{198}Hg, studying the evolution of the system's preference for symmetry or asymmetry with temperature. We finally evaluated the performance of the new functional, UNEDF1, in predicting fission-related quantities across the actinide region.

6.1 Third Minima in Thorium and Uranium

A well-formed third minimum is present in the fission barriers of ^{232}Th calculated by most macroscopic-microscopic approaches, as well as the barriers inferred from experiments. The fission barriers calculated with self-consistent models, however, present a flat plateau rather than a clear third potential well. This contrast called for a deeper investigation: what physical effects influence the depth or presence of the third minimum?

We studied two-dimensional potential energy surfaces for ^{228,232}Th and ^{232}U at several excitation energies to observe the evolution of the balance between pairing effects and shell effects. It is well-known that the fission yield of a system becomes

more symmetric as excitation energy increases. The two Th isotopes and ^{232}U see a reduction in the barrier to symmetric fission as excitation energy increases.

To further elucidate the microscopic drivers, we compared several isotopes of Th and U, especially the isotopes with smaller neutron number that possess clear third minima at zero excitation energy. The main common effect appears to be a large hump in the neutron shell correction energy, which creates the third barrier and thus the third minimum.

For the actinides, the asymmetry of the fission yields has long been related to the fact that one of the fragments tends to be close to the doubly-magic ^{132}Sn. Indeed, the hyperdeformed isomer in the third minimum has been thought to be a "molecular" configuration of two clusters, with the larger, spherical cluster being ^{132}Sn. It is possible that the past macroscopic-microscopic studies overestimated the stabilization given by shell correction energy – but if that is the case, and the third minimum is as shallow as these self-consistent calculations predict, then an alternative accounting of the experimentally observed cross section resonances is necessary.

6.2 Fission in Mercury Isotopes

Since the doubly-magic ^{132}Sn fragment was thought to be a major driver for the asymmetric fission of the actinides, the experimental discovery that the most likely fission yield of ^{180}Hg is *not* two semi-magic ^{90}Zr fragments came as a surprise. A more careful examination of the potential energy surface and shell correction energies does reveal that subtle shell effects drive ^{180}Hg to asymmetric fission, while ^{198}Hg tends towards symmetric fission.

To more accurately model the experimental situation in which nuclei are excited, we performed the first FT-DFT study of the potential energy surfaces of ^{180}Hg and ^{198}Hg at several excitation energies. We found that ^{180}Hg evolves with excitation energy in a manner similar to Th and ^{232}U – the system begins to prefer a symmetric fission pathway as the barrier to this pathway is gradually lowered.

The potential energy surface of ^{198}Hg, which reveals a preference for rather small asymmetric deformation at $E^* = 0$MeV, very quickly favors symmetric fission as excitation energy increases.

The theoretical picture of ^{180}Hg that has been emerging since the experimental discovery of its asymmetric fission mode demonstrates subtleties not immediately obvious from past fission studies in the actinides. A thorough analysis of the potential energy surface was needed to reliably predict the most likely fission path for the mercury isotopes. The transition with neutron number from asymmetric fission in ^{180}Hg to symmetric fission in ^{198}Hg illustrates an intricacy of nuclear fission that must be capture by any reliable theory. That the FT-DFT fission model, whose only input is the nuclear force parametrization, captures these salient features is highly encouraging.

6.3 Survey of Spontaneous Fission in the Actinides

We turned then from specific cases to a general survey of the actinide region. Our systematic comparison of the UNEDF1 fission barriers with those of experiment as well as other theoretical approaches shows that the UNEDF1 functional is competitive with the best approaches to fission.

It is valuable to see that several microscopic approaches to fission produce fission barrier predictions of a quality similar to macroscopic-microscopic approaches. Since no fission data were incorporated into the optimization procedure for UNEDF1, this represents a significant step towards a truly predictive, microscopic theory of fission.

The agreement between the empirical barrier heights and those predicted using UNEDF1 is encouraging, especially combined with the quality of the half-lives predicted using UNEDF1 and the ATDHFB theory. The collective inertias calculated self-consistently with UNEDF1 did require a phenomenological correction to obtain realistic half-lives, suggesting that static barrier heights alone do not determine the dynamics of the fission process. Furthermore, while reducing the

problem of fission to a semi-classical, one-dimensional barrier penetration problem presents a strong backbone for spontaneous fission half-life predictions, more remains to be learned about the dynamics of fission. Time-odd terms in the collective inertia will be an important development. Additionally, treatments that go beyond the semi-classical treatment of the fission pathway, such as with path integrals, also represent a good goal for future endeavors.

6.4 Summary and Prospects

Through our survey of the actinides and our focused study of thorium, uranium, and mercury isotopes, we have assessed the capabilities of the nuclear density functional theory for reliable predictions of fission observables. We have seen the value of the finite-temperature DFT theory for compound nuclei with excitation energy. We have also seen the merits of the ATDHFB theory for the study of spontaneous fission.

To understand the fission of the nucleus with a theoretical framework based solely on the microscopic EDF is a grand challenge. This study has presented aspects in which our model of nuclear fission has been enhanced by an improved description of the effective nuclear interaction. This microscopic model yields results of a fidelity competitive with the best macroscopic-microscopic methods. Since the microscopic model of the nuclear force is rooted in the properties of nuclear matter itself, we have reason to be confident in the predictions of this model beyond known data.

Chapter 7

Specific Contributions

This dissertation is concluded with a list of the author's specific contributions to the work presented here.

- Computational Methods
  - Helped prepare the MPI functionality of the code HFODD for use with fission
  - Implemented ScaLAPACK diagonalization routines in HFODD
  - Compared the performance of ScaLAPACK diagonalization and threaded LAPACK
  - Visualization for nuclear potential energy surfaces
  - Visualization for one-proton quasiparticle excitations
- Calculations for Fission
  - Large-scale computations of potential energy surfaces for major actinides, minor actinides, and mercury isotopes with the Jaguar Cray XT5 and the Kraken XT5
  - Calculations of spontaneous fission half-lives for major and minor actinides

- Expanded scope of the study of third minima for ^{232}Th and ^{232}U to include lighter isotopes of both elements

- Publications

  - M. Kortelainen, J. McDonnell, W. Nazarewicz, P.-G. Reinhard, J. Sarich, N. Schunck, M.V. Stoitsov, S.M. Wild. "Nuclear energy density optimization. III. UNEDF2" (*in preparation*).

  - J.D. McDonnell *et al.* "Systematic Study of Spontaneous Fission in the Actinides" (*in preparation*).

  - J.D. McDonnell *et al.* "Microscopic Study of the Fission of Mercury Isotopes at Finite Temperature" (*in preparation*).

  - J.D. McDonnell *et al.* "Microscopic Study of Third Minima in Thorium and Uranium Isotopes" (*in preparation*).

  - M. Kortelainen, J. McDonnell, W. Nazarewicz, P.-G. Reinhard, J. Sarich, N. Schunck, M.V. Stoitsov, S.M. Wild. "Nuclear energy density optimization. II. Large deformations", *Phys. Rev.* **C85**, 024304 (2012).

  - N. Schunck, J. Dobaczewski, J. McDonnell, W. Satula, J.A. Sheikh, A. Staczszak, M. Stoitsov, P. Toivanen. "Solution of the Skyrme-Hartree-Fock-Bogolyubov equations in the Cartesian deformed harmonic-oscillator basis. (VII) hfodd (v2.49t): a new version of the program", *Comp. Phys. Comm.* **183**, 166 (2012).

  - W. Nazarewicz and J. McDonnell. "Towards Predictive Theory of Fission", *Stewardship Science Academic Alliances Annual 2011*, DOE/NA-0016, p.18 (2011).

  - N. Schunck, J. Dobaczewski, J. McDonnell, J. More, W. Nazarewicz, J. Sarich, and M. V. Stoitsov. "One-quasiparticle states in the nuclear energy density functional theory", *Phys. Rev.* **C81**, 024316 (2010).

- J.D. McDonnell, W. Nazarewicz, J.A. Sheikh, "Thermal Fission Pathways in 232Th", 4th International Workshop on Fission and Fission Product Spectroscopy, *AIP Conference Proceedings*, Volume 1175, pp. 371-374 (2009).

- Presentations at Meetings

  - "Nuclear Fission: From Microscopic Forces to Experimental Observables", poster, J. McDonnell, W. Nazarewicz, M. Kortelainen, N. Schunck, J.A. Sheikh, M.V. Stoitsov, Stewardship Science Academic Alliance Symposium, Washington, D.C., February 22-23, 2012. *Recognized by an "Outstanding Poster Award".*

  - "Fission of Actinide Nuclei", J. McDonnell, M. Kortelainen, W. Nazarewicz, J.A. Sheikh, M.V. Stoitsov, N. Schunck, FUSTIPEN Topical Meeting on 'Theory of Nuclear Fission' at GANIL, Caen, France, January 4 6, 2012.

  - "Fission of Actinide Nuclei", J. McDonnell, M. Kortelainen, W. Nazarewicz, J.A. Sheikh, M.V. Stoitsov, N. Schunck, Fall Meeting of the American Physical Society Division of Nuclear Physics, East Lansing, MI, October 26 29, 2011.

  - "Fission Barriers in Actinide Nuclei", J. McDonnell, M. Kortelainen, W. Nazarewicz, J.A. Sheikh, M.V. Stoitsov, 5th LACM-EFES-JUSTIPEN Workshop, Oak Ridge, TN, March 15-17, 2011.

  - "Understanding Nuclear Reactions", poster, J. McDonnell, W. Nazarewicz, Stewardship Science Graduate Fellowship Annual Meeting, Washington, D.C., July 20 - 22, 2011.

  - "Microscopic Description of Fission Process", W. Nazarewicz, J. McDonnell, Stewardship Science Academic Alliance Symposium, Washington, D.C., February 14-17, 2011.

– "Third Minima in Actinide Nuclei", poster, J .D. McDonnell, W. Nazarewicz, N. Schunck, J.A. Sheikh, Stewardship Science Center External Review, Oak Ridge, TN, December 2, 2010.

– "Analyzing Powers for 3H(d,n)4He from *ab initio* NCSM+RGM: A Study of the Deuterium-Tritium Fusion Reaction", J. McDonnell, P. Navratil, E. Ormand, S. Quaglioni, Summer Student Presentation for Stewardship Science Graduate Fellowship Practicum, Lawrence Livermore National Laboratory, Livermore, CA, August 6, 2010.

– "Thermal Fission Barriers for Thorium-232 in Two Collective Coordinates", poster, J.D. McDonnell, W. Nazarewicz, N. Schunck, and J.A. Sheikh, Stewardship Science Graduate Fellowship Annual Conference, Washington, D.C., June 21, 2010.

– "Microscopic Study of Fission in Two Collective Coordinates", 4th LACM-EFES-JUSTIPEN Workshop, Oak Ridge, TN, March 15, 2010.

– "Nuclear Fission at Finite Temperature", poster, J.D. McDonnell, W. Nazarewicz, J.A. Sheikh, National Nuclear Physics Summer School, East Lansing, MI, June 28 July 10, 2009.

– "Nuclear Fission at Finite Temperature", poster, J.D. McDonnell, W. Nazarewicz, J.A. Sheikh, 4th International Conference on Fission and Fission Product Spectroscopy, Cadarache, France, May 13-16, 2009.

– "Visualization and Analysis of Nuclear Quasi-Particle States", poster, J.D. McDonnell, W. Nazarewicz, M.Stoitsov, N. Schunck, CNS-EFES08 Summer School, Tokyo, Japan, Aug. 28, 2008.

Bibliography

Bibliography

Andreyev, A. *et al.*, 2010, Phys. Rev. Lett. 105, 252502. 4, 6, 39

Asghar, M., 1978, Z. Phys. A 286, 299–300. 5

Baran, A., J. Sheikh, and W. Nazarewicz, 2009, Int. J. Mod. Phys. E 18, 1054–1057. 54

Baran, A., J. A. Sheikh, J. Dobaczewski, W. Nazarewicz, and A. Staszczak, 2011, Phys. Rev. C 84, 054321. 19, 20, 21

Baran, A., A. Staszczak, J. Dobaczewski, and W. Nazarewicz, 2007, Int. J. Mod. Phys. E 16, 443–451. 19

Baranger, M. and M. Veneroni, 1978, Ann. Phys. 114, 123–200. 20, 76

Bender, M., P.-H. Heenen, and P.-G. Reinhard, 2003, Rev. Mod. Phys. 75, 121. 2, 8, 10

Berger, J., M. Girod, and D. Gogny, 1989, Nuc. Phys. A 502, 85. 5, 24

Bjørnholm, S. and J. Lynn, 1980, Rev. Mod. Phys. 52, 725. 3, 18, 23

Blokhin, A. and A. Soldatov, 2009, Phys. At. Nuc. 72, 917–927. 5

Blons, J., 1989, Nuc. Phys. A 502, 121c–140c. 23

Blons, J., B. Fabbro, C. Mazur, D. Paya, M. Ribrag, and Y. Patin, 1988, Nuc. Phys. A 477, 231–255. 5

Blons, J., C. Mazur, D. Paya, M. Ribrag, and H. Weigmann, 1984, Nuc. Phys. A 414, 1–41. 23

Bogner, S., R. Furnstahl, and A. Schwenk, 2010, Prog. Part. Nucl. Phys. 65, 94–147. 1

Bohr, N. and J. A. Wheeler, 1939, Phys. Rev. 56, 426–450. 1

Bonneau, L., P. Quentin, and D. Samsoen, 2004, Eur. Phys. J. A 21, 391–406. 5, 24

Brack, M., J. Damgaard, A. Jensen, H. Pauli, V. Strutinski, and C. Wong, 1972, Rev. Mod. Phys. 44, 320. 1, 4

Browne, E., 2006, Nuclear Data Sheets 107, 2579–2648. 35

Capote, R. *et al.*, 2009, Nuclear Data Sheets 110, 3107. 35, 49, 50

Csige, L. *et al.*, 2009, Phys. Rev. C 80, 011301(R). 23, 29

Cwiok, S., J. Dudek, W. Nazarewicz, J. Skalski, and T. Werner, 1987, Comp. Phys. Comm. 46, 379–399. 2

Ćwiok, S., W. Nazarewicz, J. Saladin, W. Plóciennik, and A. Johnson, 1994, Phys. Lett. B 322, 304–310. 2, 4, 24

Dechargé, J. and D. Gogny, 1980, Phys. Rev. C 21, 1568. 9

Delaroche, J.-P., M. Girod, H. Goutte, and J. Libert, 2006, Nuc. Phys. A 771, 103–168. 4, 49, 50

Dobaczewski, J., H. Flocard, and J. Treiner, 1984, Nuc. Phys. A 422, 103–139. 12

Dobaczewski, J. and P. Olbratowski, 2004, Comp. Phys. Comm. 158, 158–191. 16, 18

Dobaczewski, J., W. Satuła, B. Carlsson, J. Engel, P. Olbratowski, P. Powałowski, M. Sadziak, J. Sarich, N. Schunck, A. Staszczak, M. Stoitsov, M. Zalewski, and H. Zduńczuk, 2009, Comp. Phys. Comm. 180, 2361–2391. 12

Dutra, M., O. Lourenço, J. S. Sá Martins, A. Delfino, J. R. Stone, and P. D. Stevenson, 2012, Phys. Rev. C 85, 035201. 3

Egido, J., P. Ring, and H. Mang, 1986, Nuc. Phys. A 451, 77–90. 14

Goodman, A., 1981, Nuc. Phys. A 352, 30–44. 14

Goutte, H., J. Berger, P. Casoli, and D. Gogny, 2005, Phys. Rev. C 71, 024316. 20

Günther, W., K. Huber, U. Kneissl, H. Krieger, and H. Maier, 1980, Z. Phys. A 295, 333–340. 28

Hagen, G., T. Papenbrock, D. J. Dean, and M. Hjorth-Jensen, 2010, Phys. Rev. C 82, 034330. 2

Hebeler, K., S. Bogner, R. Furnstahl, A. Nogga, and A. Schwenk, 2011, Phys. Rev. C 83, 031301(R). 3

Hinohara, N., Z. P. Li, T. Nakatsukasa, T. Nikšić, and D. Vretenar, 2012, Phys. Rev. C 85, 024323. 21

Holden, N. and D. Hoffman, 2000, Pure Appl. Chem. 72, 1525–1562. 55

Ichikawa, T., A. Iwamoto, P. Möller, and A. Sierk, 2012, arXiv 1203.2011v2. 39

Kortelainen, M., T. Lesinski, J. Moré, W. Nazarewicz, J. Sarich, N. Schunck, M. V. Stoitsov, and S. Wild, 2010, Phys. Rev. C 82, 2, 024313. 1, 10

Kortelainen, M., J. McDonnell, W. Nazarewicz, P.-G. Reinhard, J. Sarich, N. Schunck, M. V. Stoitsov, and S. M. Wild, 2012, Phys. Rev. C 85, 024304. 6, 7, 10, 11, 45

Kowal, M. and J. Skalski, 2012, Phys. Rev. C 85, 061302. 4, 5, 24, 30

Krappe, H. and K. Pomorski, 2012, *Theory of Nuclear Fission* (Springer). 1

Krasznahorkay, A., D. Habs, M. Hunyadi, D. Gassmann, M. Csatlós, Y. Eisermann, T. Faestermann, G. Graw, J. Gulyás, R. Hertenberger, H. Maier, Z. Máté, A. Metz, J. Ott, P. Thirolf, and S. van der Werf, 1999, Phys. Lett. B 461, 15–21. 5

Krieger, S. and K. Goeke, 1974, Nuc. Phys. A 234, 269–284. 20, 76

Libert, J., M. Girod, and J.-P. Delaroche, 1999, Phys. Rev. C 60, 054301. 20, 21

Lu, B.-N., E.-G. Zhao, and S.-G. Zhou, 2012, Phys. Rev. C 85, 011301. 46, 56

McDonnell, J., W. Nazarewicz, and J. Sheikh, 2009, in "Proc. 4th International Workshop on Fission and Fission Product Spectroscopy," *AIP Conf. Proc.*, vol. 1175, pp. 371–374. 5

Mirea, M. and L. Tassan-Got, 2009, in "Proc. 4th International Workshop on Fission and Fission Product Spectroscopy," *AIP Conf. Proc.*, vol. 1175, pp. 219–226. 38

Mirea, M., L. Tassan-Got, C. Stephan, C. O. Bacri, and R. C. Bobulescu, 2007, Phys. Rev. C 76, 064608. 19

Möller, P., D. Madland, A. Sierk, and A. Iwamoto, 2001, Nature 409, 785–790. 2, 4

Möller, P., W. D. Myers, H. Sagawa, and S. Yoshida, 2012a, Phys. Rev. Lett. 108, 052501. 2

Möller, P., S. Nilsson, and R. Sheline, 1972, Phys. Lett. B 40, 329. 4

Möller, P., J. Randrup, and A. J. Sierk, 2012b, Phys. Rev. C 85, 024306. 2, 39

Möller, P. *et al.*, 2009, Phys. Rev. C 79, 064304. 2, 4, 49, 50

Navrátil, P. and S. Quaglioni, 2011, Phys. Rev. C 83, 044609. 2

Nazarewicz, W., 1993, Nuclear Physics A 557, 489–514. 15, 26, 38

Negele, J., 1989, Nuc. Phys. A 502, 371c–386c. 19, 21

Nikolov, N., N. Schunck, W. Nazarewicz, M. Bender, and J. Pei, 2011, Phys. Rev. C 83, 034305. 13

Pei, J., W. Nazarewicz, J. Sheikh, and A. Kerman, 2009, Phys. Rev. Lett. 102, 192501. 4, 15

Ring, P. and P. Schuck, 1980, *The Nuclear Many-Body Problem* (Springer). 1, 2, 11, 13

Schunck, N., J. Dobaczewski, J. McDonnell, W. Satuła, J. Sheikh, A. Staszczak, M. Stoitsov, and P. Toivanen, 2012, Comp. Phys. Comm. 183, 166–192. 13, 18

Sheikh, J., W. Nazarewicz, and J. Pei, 2009, Phys. Rev. C 80, 011302. 15

Singh, B., R. Zywina, and R. B. Firestone, 2002, Nuclear Data Sheets 97, 2, 241–592. 4, 23, 52

Skalski, J., 2008, Phys. Rev. C 77, 064610. 19, 21

Smirenkin, G., 1993, Tech. Rep. 359, INDC(CCP). 49, 50

Staszczak, A., M. Stoitsov, A. Baran, and W. Nazarewicz, 2010, Eur. Phys. J. A pp. 1–6. 16

Stoitsov, M., M. Kortelainen, S. K. Bogner, T. Duguet, R. J. Furnstahl, B. Gebremariam, and N. Schunck, 2010, Phys. Rev. C 82, 054307. 1

Stone, J. and P.-G. Reinhard, 2007, Prog. Part. Nuc. Phys. 58, 587–657. 3, 10

Thirolf, P. G. and D. Habs, 2002, Prog. Part. Nuc. Phys. 49, 325–402. 5

Vautherin, D. and D. Brink, 1972, Phys. Rev. C 5, 626–647. 9

Vertse, T., A. T. Kruppa, and W. Nazarewicz, 2000, Phys. Rev. C 61, 064317. 13

Viola, V. and G. Seaborg, 1966, J. Inorg. Nuc. Chem. 28, 741–761. 3

Warda, M., A. Staszczak, and W. Nazarewicz, 2012, arXiv 1205.5797v1. 39

Younes, W. and D. Gogny, 2009, Phys. Rev. C 80, 054313. 17

Yuldashbaeva, E., J. Libert, P. Quentin, and M. Girod, 1999, Phys. Lett. B 461, 1–8. 20

Appendix

Appendix A

More on ATDHFB

In this Appendix, we review a method to derive the expression for the collective inertia needed for fission dynamics and the calculation of such quantities as the spontaneous fission half-life.

To properly include pairing, a double-space density operator is employed,

$$\mathcal{R} = \begin{bmatrix} \rho & -\kappa \\ \kappa^* & 1-\rho^* \end{bmatrix}, \tag{A.1}$$

with ρ the normal density operator and κ the pairing tensor as usual. The HFB Hamiltonian for this space keeps the form

$$\mathcal{H} = \begin{bmatrix} h & \Delta \\ -\Delta^* & -h^* \end{bmatrix}. \tag{A.2}$$

The double-space density operator is expressed in terms of a "position" coordinate $\mathcal{R}_0$ and a "momentum" coordinate $\chi(t)$,

$$\mathcal{R}(t) = e^{i\chi(t)}\mathcal{R}_0 e^{-i\chi(t)}.$$

The adiabatic approximation assumes small momenta, so that terms higher than second order in χ are neglected. The expansion yields

$$\begin{aligned}\mathcal{R} &\approx \left(1 + i\chi - \frac{1}{2}\chi^2\right)\mathcal{R}_0\left(1 - i\chi - \frac{1}{2}\chi^2\right) \\ &\approx \mathcal{R}_0 + i\left[\chi, \mathcal{R}_0\right] - \frac{1}{2}\left[\chi, [\chi, R_0]\right] \\ &= \mathcal{R}_0 + \mathcal{R}_1 + \mathcal{R}_2, \end{aligned} \tag{A.3}$$

where the last line defines the terms of the expansion of $\mathcal{R}$ as commutators of the corresponding orders of χ.

There is a property of the χ functions that produces the identities

$$\mathcal{R}_0\chi\mathcal{R}_0 = 0; \quad (1 - \mathcal{R}_0)\chi(1 - \mathcal{R}_0) = 0.$$

Manipulation of the second identity with the knowledge of the first identity yields a relation for χ,

$$(1 - \mathcal{R}_0)\chi(1 - \mathcal{R}_0) = \chi + \mathcal{R}_0\chi\mathcal{R}_0 - \mathcal{R}_0\chi - \chi\mathcal{R}_0,$$

so that

$$\chi = \mathcal{R}_0\chi + \chi\mathcal{R}_0. \tag{A.4}$$

We can consider the definition of $\mathcal{R}_1$ to obtain χ in terms of the $\mathcal{R}$'s,

$$\mathcal{R}_1 = i\left[\chi, \mathcal{R}_0\right] = i\chi\mathcal{R}_0 - i\mathcal{R}_0\chi.$$

After multiplying one copy of the equation on the left by $\mathcal{R}_0$, and a second copy on the right by $\mathcal{R}_0$, we use the identities above and subtract to obtain

$$\mathcal{R}_1\mathcal{R}_0 - \mathcal{R}_0\mathcal{R}_1 = i(\chi\mathcal{R}_0 + \mathcal{R}_0\chi) = i\chi,$$

so that

$$\chi = i\left[\mathcal{R}_0, \mathcal{R}_1\right]. \tag{A.5}$$

The double space HFB Hamiltonian may be written

$$\mathcal{H} = \mathcal{T} + \frac{1}{2}\mathrm{Tr}\mathcal{V}\mathcal{R}, \tag{A.6}$$

where $\mathcal{T}$ is a matrix representing kinetic energy contributions and $\mathcal{V}$ is a matrix representing potential energy. An adiabatic expansion of the Hamiltonian may be obtained by substituting the expansion of $\mathcal{R}$.

We know that the time derivative of $\mathcal{R}$ is related to its commutator with the Hamiltonian,

$$i\dot{\mathcal{R}} = \left[\mathcal{H}, \mathcal{R}\right],$$

into which the adiabatic expansions may be substituted. Collection of time-even (even-order in χ) and time-odd (odd-order in χ) yields the system of ATDHFB equations,

$$\begin{aligned} i\dot{\mathcal{R}}_0 &= \left[\mathcal{H}_0, \mathcal{R}_1\right] + \left[\mathcal{H}_1, \mathcal{R}_0\right], \\ i\dot{\mathcal{R}}_1 &= \left[\mathcal{H}_0, \mathcal{R}_0\right] + \left[\mathcal{H}_1, \mathcal{R}_1\right] + \left[\mathcal{H}_2, \mathcal{R}_0\right] + \left[\mathcal{H}_0, \mathcal{R}_2\right]. \end{aligned}$$

In practice, $\mathcal{R}_0$ is obtained by the solution of the usual HFB equations, and the first of these ATDHFB equations is sufficient to solve for $\mathcal{R}_1$.

The expectation value of the energy is obtained by calculating

$$E = \frac{1}{2}\mathrm{Tr}\mathcal{H}\mathcal{R}. \tag{A.7}$$

Upon the adiabatic expansion of the total energy, the kinetic energy is identified as the second order term, proportional to χ^2. With the identification that the kinetic energy takes the form

$$\mathcal{K} = \frac{1}{2}\mathcal{M}\dot{q}^2,$$

we find that the collective inertia $\mathcal{M}$ is obtained through the calculation of the system's kinetic energy.

With the adiabatic expansion, we have for the second order terms (Krieger and Goeke, 1974)

$$\begin{aligned}\mathcal{K} = E^{(2)} &= \frac{1}{2}\mathrm{Tr}\mathcal{T}\mathcal{R}_2 + \frac{1}{8}\mathrm{Tr}\mathcal{V}\left(\mathcal{R}_0\mathcal{R}_2 + \mathcal{R}_1\mathcal{R}_1 + \mathcal{R}_2\mathcal{R}_0\right) \\ &= \frac{1}{2}\mathrm{Tr}\left[\left(\mathcal{T} + \frac{1}{2}\mathrm{Tr}\mathcal{R}_0\mathcal{V}\right)\mathcal{R}_2\right] - \frac{1}{8}\mathrm{Tr}\mathcal{R}_0\mathcal{V}\mathcal{R}_2 + \frac{1}{8}\mathrm{Tr}\mathcal{R}_1\mathcal{V}\mathcal{R}_1 + \frac{1}{8}\mathrm{Tr}\mathcal{R}_2\mathcal{V}\mathcal{R}_0 \\ &= \frac{1}{2}\mathrm{Tr}\mathcal{H}_0\mathcal{R}_2 + \frac{1}{4}\mathrm{Tr}\mathcal{H}_1\mathcal{R}_1,\end{aligned}$$

where the final line substituted the definitions of $\mathcal{H}_i$ from the adiabatic expansion.

With some manipulation, the Hamiltonian matrices may be eliminated to leave an expression for the kinetic energy solely in terms of the expansion of the density operator. We use the definitions of $\mathcal{R}_1$ and $\mathcal{R}_2$ to find some helpful identities:

$$\begin{aligned}\mathcal{R}_1 &= i\left[\chi, \mathcal{R}_0\right]; \\ \mathcal{R}_2 &= -\frac{1}{2}\left[\chi, \left[\chi, \mathcal{R}_0\right]\right] = \frac{1}{2}i\left[\chi, \mathcal{R}_1\right].\end{aligned}$$

The kinetic energy becomes

$$\begin{aligned}\mathcal{K} &= \frac{i}{4}\mathrm{Tr}\left(\mathcal{H}_0\left[\chi, \mathcal{R}_1\right]\right) + \frac{i}{4}\mathrm{Tr}\left(\mathcal{H}_1\left[\chi, \mathcal{R}_0\right]\right) \\ &= -\frac{i}{4}\mathrm{Tr}\left\{\left(\left[\mathcal{H}_0, \mathcal{R}_1\right] + \left[\mathcal{H}_1, \mathcal{R}_0\right]\right)\chi\right\} \\ &= \frac{1}{4}\mathrm{Tr}\left(\dot{\mathcal{R}}_0\chi\right) \\ &= \frac{i}{4}\mathrm{Tr}\left(\dot{\mathcal{R}}_0\left[\mathcal{R}_0, \mathcal{R}_1\right]\right), \qquad \text{(A.8)}\end{aligned}$$

where the second step used the property of traces of products, and the third step used the first ATDHFB equation.

We see here the relationship between the kinetic energy and the "momentum" coordinate of Baranger and Veneroni (1978).

Since the kinetic energy has the form

$$\mathcal{K} = \frac{1}{2}\mathcal{M}\dot{q}^2,$$

we solve to find the expression for the collective inertia,

$$\mathcal{M} = \frac{i}{2\dot{q}^2}\mathrm{Tr}\left(\dot{\mathcal{R}}_0\left[\mathcal{R}_0, \mathcal{R}_1\right]\right). \tag{A.9}$$

This expression is quite general, but already cannot be generalized to a finite-temperature formalism (in which $\mathcal{R}^2 \neq \mathcal{R}$, as required subtly in this brief derivation).

Appendix B

Tables of Predictions for Spontaneous Fission in the Actinides

In this Appendix, we present numerical tables for the actinide fission barrier heights, isomeric energies, and spontaneous fission half-lives predicted using various functionals. We present empirical values alongside the predictions where available. These tables correspond to the graphics in Chapter 5, Sections 5.3 and 5.4.

Table B.1: For each theoretical model, the first barrier height E_A is displayed, in MeV.

	Exp.	UNEDF1	FRLDM	SkM*	D1S
^{224}Ra	-	4.78	-	5.39	-
^{226}Ra	-	4.7	-	5.2	-
^{228}Ra	-	5.4	-	5.51	-
^{230}Ra	-	5.42	-	5.66	-
^{226}Th	-	4.23	3.68	4.93	3.6
^{228}Th	6.2	4.9	2.94	5.25	4.27
^{230}Th	6.1	5.62	2.65	5.72	4.8
^{232}Th	5.8	6.12	3.18	6.21	5.12
^{234}Th	6.1	6.24	3.59	6.48	5.25
^{236}Th	-	6.37	4.25	6.82	5.33
^{228}U	-	3.89	-	4.47	3.16
^{230}U	-	4.55	3.02	5.59	4.26
^{232}U	4.9	5.81	3.17	6.18	5.06
^{234}U	4.8	6.54	3.8	6.84	5.42
^{236}U	5	6.77	4.45	7.09	5.9
^{238}U	6.3	6.75	5.08	8.4	5.99
^{240}U	6.1	6.18	5.65	7.51	5.46
^{242}U	-	5.47	5.95	6.61	4.79
^{234}Pu	-	5.77	-	6.29	4.98
^{236}Pu	5.7	6.73	4.49	6.92	5.39
^{238}Pu	5.6	6.95	5.27	7.3	6.43
^{240}Pu	6.05	7.07	5.99	7.44	6.64
^{242}Pu	5.85	7.72	6.42	7.81	6.03
^{244}Pu	5.7	6.36	6.59	8.54	5.31
^{246}Pu	5.4	5.34	6.34	6.57	4.61
^{248}Pu	-	4.84	-	5.82	-
^{242}Cm	6.65	7.23	6.56	7.62	6.49
^{244}Cm	6.18	7.01	6.92	7.71	6.29
^{246}Cm	6	6.9	7.01	8.13	5.6
^{248}Cm	5.8	7.29	6.8	8.04	5.26
^{250}Cm	5.4	5.57	5.87	6.31	5.08
^{242}Cf	-	6.76	-	7.4	5.74
^{244}Cf	-	7.23	-	7.92	5.95
^{246}Cf	-	7.01	7.15	8.07	5.94
^{248}Cf	-	7.07	7.24	7.99	5.96
^{250}Cf	5.6	6.81	7.09	7.54	6.03
^{252}Cf	5.4	6.19	6.07	6.87	5.4

Table B.2: For each theoretical model, the fission isomer energy E_{II} is displayed, in MeV.

	Exp.	UNEDF1	FRLDM	SkM*	D1S
^{224}Ra	-	4.12	-	4.91	-
^{226}Ra	-	3.5	-	4.13	-
^{228}Ra	-	2.3	-	3.41	-
^{230}Ra	-	1.39	-	2.74	-
^{226}Th	-	3.97	4.24	4.46	3.57
^{228}Th	-	3.68	3.43	4.16	3.67
^{230}Th	-	2.92	3.1	3.68	3.17
^{232}Th	-	2.27	2.79	3.11	2.38
^{234}Th	-	2.29	2.34	2.7	1.92
^{236}Th	-	2.18	2.39	2.44	2.19
^{228}U	-	2.79	-	3.97	3.12
^{230}U	-	3.58	3.52	4.06	3.62
^{232}U	-	3.17	3.39	3.78	3.29
^{234}U	-	2.74	3.22	3.39	2.72
^{236}U	2.75	2.67	2.87	2.97	2.45
^{238}U	2.557	3.04	2.85	3.18	2.6
^{240}U	-	2.82	2.92	2.69	2.48
^{242}U	-	2.96	3.33	2.41	2.59
^{234}Pu	-	2.71	-	3.36	2.81
^{236}Pu	-	2.42	3.22	3.09	2.48
^{238}Pu	2.4	2.46	2.99	2.91	2.61
^{240}Pu	2.8	2.71	2.94	2.67	2.81
^{242}Pu	2.2	2.88	3.07	2.52	2.75
^{244}Pu	2.4	2.91	3.45	2.52	2.71
^{246}Pu	-	2.79	3.86	2.31	2.65
^{248}Pu	-	2.55	-	2.15	-
^{242}Cm	1.9	2.07	2.78	2.29	2.42
^{244}Cm	2.2	2.34	2.94	2.25	2.54
^{246}Cm	-	2.41	3.5	2.19	2.57
^{248}Cm	-	2.24	3.95	2.03	2.49
^{250}Cm	-	1.88	3.71	1.82	2.32
^{242}Cf	-	0.27	-	1.39	0.94
^{244}Cf	-	0.85	-	1.56	1.53
^{246}Cf	-	1	2.7	1.65	1.97
^{248}Cf	-	1.3	3.38	1.72	2.23
^{250}Cf	-	1.33	3.87	1.59	2.15
^{252}Cf	-	1.16	3.55	1.29	1.68

Table B.3: For each theoretical model, the second barrier height E_B is displayed, in MeV.

	Exp.	UNEDF1	FRLDM	SkM*	D1S
^{224}Ra	-	8.19	8.78	9.35	-
^{226}Ra	8.5	7.65	8.23	8.48	-
^{228}Ra	8	7.26	7.61	7.89	-
^{230}Ra	-	7.39	7.04	7.76	-
^{226}Th	-	7.15	7.2	7.42	7
^{228}Th	6.5	6.5	6.53	7.36	7
^{230}Th	6.8	6.38	5.55	7.33	6.43
^{232}Th	6.7	6.29	5.45	7.28	6.52
^{234}Th	6.3	6.63	5.37	7.47	6.94
^{236}Th	-	7.67	6.04	7.88	7
^{228}U	-	5	-	6.05	5.95
^{230}U	-	5.65	4.28	6.61	5.83
^{232}U	5.4	5.41	4.73	6.57	5.33
^{234}U	5.5	5.44	4.89	6.65	5.72
^{236}U	5.67	5.77	5.03	6.85	6.27
^{238}U	5.5	6.76	5.64	7.84	7
^{240}U	5.8	6.4	6.37	7.93	7
^{242}U	-	6.53	7.1	7.94	7
^{234}Pu	-	3.98	-	5.39	4.25
^{236}Pu	4.5	4.45	4.36	5.86	4.5
^{238}Pu	5.1	4.65	4.47	5.92	5.53
^{240}Pu	5.15	5.43	4.91	6.43	6.71
^{242}Pu	5.05	6.22	5.72	6.97	7
^{244}Pu	4.85	6.62	6.47	7.41	7
^{246}Pu	5.3	5.43	7.07	7.15	7
^{248}Pu	-	5.1	-	6.9	-
^{242}Cm	5	4.1	4.45	5.32	5.47
^{244}Cm	5.1	5.03	5.07	5.88	6.16
^{246}Cm	4.8	5.51	5.87	6.2	6.71
^{248}Cm	4.8	5.64	6.65	6.47	6.71
^{250}Cm	4.4	4.04	6.25	5.96	4.84
^{242}Cf	-	2.42	-	3.73	2.47
^{244}Cf	-	3.01	-	4.24	3.55
^{246}Cf	-	3.44	4.34	4.65	4.7
^{248}Cf	-	4.26	5.18	5.03	5.05
^{250}Cf	3.8	3.38	5.92	5.11	4.68
^{252}Cf	3.5	2.71	5.83	4.87	3.3

Table B.4: For UNEDF1 and SkM*, the logarithm of the spontaneous fission half-life $\log(T_{\text{s.f.}})$ is displayed, where $T_{\text{s.f.}}$ is measured in years.

	Exp.	UNEDF1	SkM*
^{226}Ra	-	42.96	42.6
^{228}Ra	-	41.92	40.8
^{230}Ra	-	-	40.37
^{226}Th	-	-	34.41
^{228}Th	-	26.36	32.92
^{230}Th	18.3	27.25	30.79
^{232}Th	21.08	28.17	32.62
^{234}Th	-	28.26	31.38
^{228}U	-	14.24	21.59
^{230}U	-	19.87	21.6
^{232}U	15.83	16.11	23.63
^{234}U	16.18	14.19	22.56
^{236}U	16.4	14.2	19.77
^{238}U	15.91	17.82	17.88
^{240}U	-	17	17.11
^{242}U	-	17.13	15.26
^{234}Pu	-	4.62	9.99
^{236}Pu	-	6.15	8.41
^{238}Pu	10.68	9.3	9.92
^{240}Pu	11.06	10.66	10.9
^{242}Pu	10.83	10.94	10.6
^{244}Pu	10.82	9.54	9
^{246}Pu	-	7.8	5.39
^{248}Pu	-	6.13	2.71
^{242}Cm	6.85	6.89	6.08
^{244}Cm	7.12	7.48	6.18
^{246}Cm	7.26	7.12	5.13
^{248}Cm	6.62	5.66	3.31
^{250}Cm	4.05	2.78	1.67
^{242}Cf	-	-0.67	-0.36
^{244}Cf	-	1.82	1.51
^{246}Cf	-	3.61	2.03
^{248}Cf	-	3.82	1.8
^{250}Cf	4.23	2.98	0.68
^{252}Cf	1.93	0	-0.95

Vita

Jordan David McDonnell, son of Jeffrey and Kimberly McDonnell, was born in Lancaster, Pennsylvania. He became interested in science and outer space at a young age, finding tidbits of astrophysics sprinkled throughout an astronomy book his father gave him. Continuing through high school and college to study physics and cosmology, he enjoyed marveling at the creation of the Almighty God, whose ways are higher than our ways, and whose thoughts are higher than our thoughts.

After studying the effects cosmological expansion would have on a solar system under Gregory Adkins, Jordan graduated *summa cum laude* with a Bachelor of Arts in Physics from Franklin and Marshall College in 2007. He then matriculated to the University of Tennessee, Knoxville, for his graduate studies. He chose to study theoretical nuclear physics under Witold Nazarewicz, interested in its applications to energy, national security, astrophysics, and the pure scientific challenge.